REPORT DOCUMENTATION PAGE

1. REPORT DATE *(DD-MM-YYYY)*	2. REPORT TYPE	3. DATES COVERED *(From - To)*

4. TITLE AND SUBTITLE

5a. CONTRACT NUMBER

5b. GRANT NUMBER

5c. PROGRAM ELEMENT NUMBER

6. AUTHOR(S)

5d. PROJECT NUMBER

5e. TASK NUMBER

5f. WORK UNIT NUMBER

7. PERFORMING ORGANIZATION NAME(S) AND ADDRESS(ES)

8. PERFORMING ORGANIZATION REPORT NUMBER

9. SPONSORING / MONITORING AGENCY NAME(S) AND ADDRESS(ES)

10. SPONSOR/MONITOR'S ACRONYM(S)

11. SPONSOR/MONITOR'S REPORT NUMBER(S)

12. DISTRIBUTION / AVAILABILITY STATEMENT

13. SUPPLEMENTARY NOTES

14. ABSTRACT

15. SUBJECT TERMS

16. SECURITY CLASSIFICATION OF:			17. LIMITATION OF ABSTRACT	18. NUMBER OF PAGES	19a. NAME OF RESPONSIBLE PERSON
a. REPORT	b. ABSTRACT	c. THIS PAGE			19b. TELEPHONE NUMBER *(include area code)*

National Hypersonic Science Center for Materials and Structures

Contract Number: FA9550-09-1-0477

Final Report

Covering the period June 1, 2009 through May 31, 2014

Prepared by:

David Marshall and Brian Cox
Teledyne Scientific Co.
1049 Camino Dos Rios
Thousand Oaks, CA 91360

Peter Kroll
University of Texas, Arlington

Greg Hilmas & William Fahrenholtz
Missouri University of Science and Technology

Rishi Raj
University of Colorado, Boulder

Robert Ritchie
University of California, Berkeley

Qingda Yang
University of Miami

Frank Zok
University of California, Santa Barbara

Prepared for:

Dr. Ali Sayir
Air Force Office of Scientific Research
875 N. Randolph Street
Arlington Virginia, 22203

Table of contents

Abstract

Research performed under the National Hypersonic Science Center for Materials and Structures (NHSC-MS) aimed to advance the basic science needed to guide design of new high-temperature oxidation-resistant ceramic materials and to develop characterization and analysis tools that enable life prediction for fiber-reinforced composites with geometrically complex microstructures. Highlights of the research are as follows:

- The roles of transition element dopants in affecting oxidation resistance of ZrB_2 ultra-high temperature ceramics, through the effects of the dopants on sintering and/or stability of the oxidation products (ZrO_2, B-O glasses, and B-Si-O glasses), were elucidated through experiments and atomistic calculations.

- Structure, oxidation behavior, and stability of HfSiCNO ceramics were determined by experiment and atomistic calculations. The potential for beneficial oxidation reactions to form "self-healing" layers containing compounds that are resistant to water vapor erosion was explored.

- Two new experimental methods were developed for characterizing fiber architectures in ceramic matrix composites and observing/measuring the evolution of damage under load at high temperatures, above 1500°C. One method uses digital surface image correlation and the other uses synchrotron x-ray micro tomography, which is capable of micron-scale resolution in 3-dimensional images.

- Under the umbrella of a virtual test system, methods were developed for: (i) analyzing 3-dimensional images of microstructures of fiber reinforced composites to create statistical characterization of the microstructure, (ii) formulation of a probabilistic generator for creating virtual specimens that replicate the measured statistics, and (iii) creation of a computational model for a virtual specimen that allows representation of discrete damage events. Computational methods included new probabilistic algorithms for generating stochastic virtual specimens and a new Augmented Finite Element Method (A-FEM) that yields extreme efficiency in dealing with arbitrary cracking in such heterogeneous materials.

1. Executive Summary: Research Organization and Outline of Topics

There is a critical need in hypersonics to develop new materials with oxidation resistance at very high temperatures and to invent approaches to combine these with fiber-reinforced composites as matrices, coatings, or in other hybrid structures. As material complexity evolves to meet the extreme challenges of hypersonics, major shortcomings are becoming evident in characterization experiments and codes for life prediction. Material failure mechanisms are obscured by the difficulty of visualizing damage during tests, especially at high temperatures. Life prediction methods must deal with multiple interacting failure mechanisms in materials that are geometrically complex and heterogeneous at multiple scales, as well as rate dependence and nonlinearity, for which current model formulations are inadequate. These are the challenges that were tackled by the NHSC-MS. Significant progress made towards establishing materials and tools to solve these challenges is summarized in the following sections.

The overall research plan is summarized in Fig. 1.1. Strong collaborations between participating institutions were enabled by the NHSC-MS and were critical to success.

The flow of information between topic areas and roles of participants are summarized in this section. The research results are then summarized in Sections 3 to 9. A list of publications resulting from the research is given in Section 10, grouped by topic area.
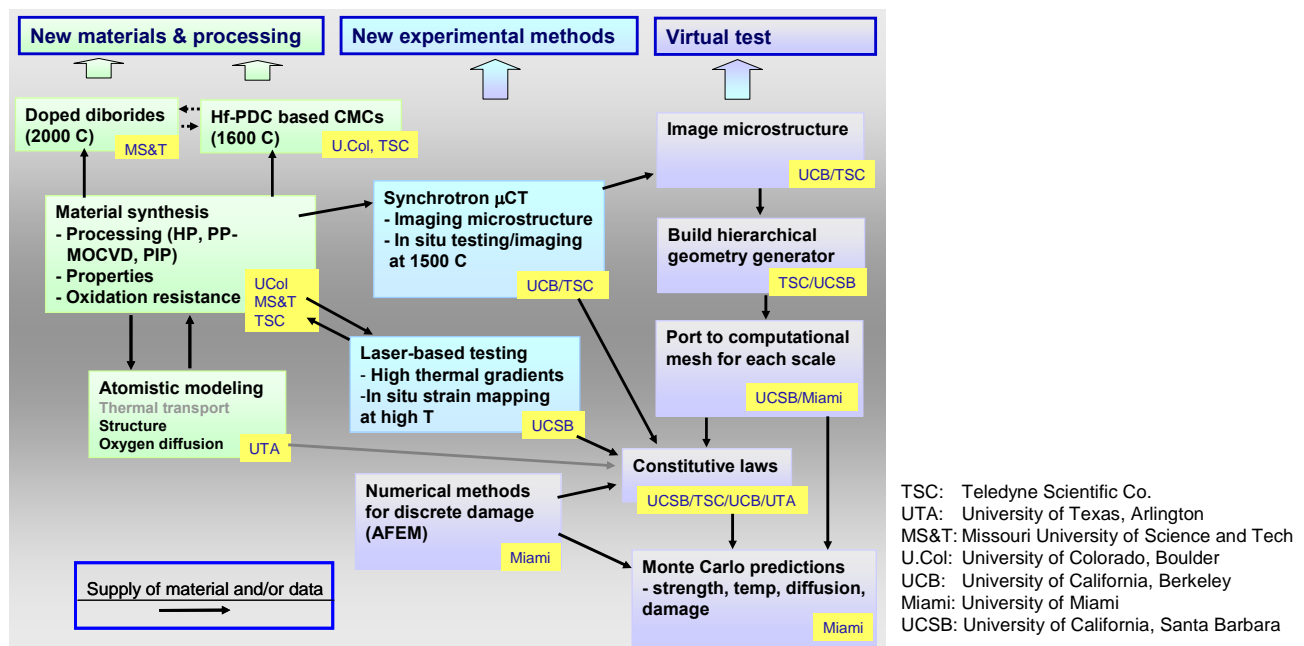

Fig. 1.1. Outline of research topics and collaborations.

2.1 Materials and Processing

Research on new materials focused on two systems. One was zirconium diboride-based materials modified by transition element dopants for improved resistance to oxidation. This system was selected on the basis of early results from Missouri University of Science and Technology

(MS&T) showing that small amounts of W dopant increased the oxidation resistance of ZrB_2. This suggested a route for potentially using doping approaches to improve the performance of these materials at very high temperatures (as needed for leading edges), above the limit for which the addition of SiC in conventional two-phase ZrB_2/SiC materials is effective. The other system involves ceramics formed from Hf-Si-C-N-O. Several attributes of this system make it an attractive candidate for use in the matrices of CMCs: the ability to process the materials via molecularly mixed preceramic polymers, the inherent oxidation resistance; and the potential for oxidation reactions to form "self-healing" layers containing compounds that are resistant to water vapor erosion.

Research on doped diborides involved collaboration between Missouri University of Science and Technology (MS&T) and the University of Texas Arlington (UTA). The MS&T group used experiments and thermodynamic modeling to explore the roles of various transition element dopants in affecting oxidation resistance through their effects on sintering and/or stability of the oxidation products (ZrO_2, B-O glasses, and B-Si-O glasses). The UTA group used atomistic calculations to explore the influence of the dopants on the structure and stability of B_2O_3 and borosilicate glasses and to determine the coordination numbers of metal cations dissolved in the glasses and implications for agglomeration and thence oxygen diffusivity.

Research on Hf-Si-C-N-O materials involved collaboration between the University of Colorado, Boulder (U.Col.), UTA and TSC. This group investigated the oxidation behavior and microstructural evolution of HfSiCNO ceramics synthesized from polymer precursors, SiC-SiC composites infiltrated with matrices formed from slurries of HfO_2 nano-particles in HfSiCNO, and mechanical/oxidation/thermal properties of HfO_2-SiC nanocomposites. Atomistic calculations (both DFT and molecular dynamics) at UTA were used to investigate the structure of amorphous SiCO materials, especially looking at the relation between composition and the dimensions of the domains formed by free-carbon segregation and the nature of bonding and interface structure between the glass and the "free" carbon phase. Diffusion of O_2 and CO in SiO_2 and SiCO glasses was studied by DFT to determine which species limits the rate of oxidation to form a layer of SiO_2 on SiCO.

C-SiC and SiC-SiC CMCs While textile-based composites with 3-D fiber architectures were the intended target for various studies in this program (new matrices, experimental test methods, and virtual test tools), the development of the fiber architectures was not a part of the program. Instead, a common representative fiber architecture, shown in Fig. 1.2 (three-layer-angle interlock woven structure), was used for all studies. C-SiC and SiC-SiC composites were fabricated at TSC. Woven fiber preforms were infiltrated first with pyrolytic carbon to provide a weak debond layer around the individual fibers, then with CVI SiC, to form a layer ~40 μm thickness, which encased the fiber tows and bonded them together where they crossed one-another to form a rigid composite. The layer of CVI SiC occupied about 20% of the volume between fiber tows. Some studies used the composite in this form. For other studies, SiC matrix material was placed into the remaining inter-tow regions by repeated cycles of infiltration and pyrolysis of slurries of SiC particles in a preceramic polymer (AHPCS). Some experiments also used unidirectional SiC-SiC composite rods consisting of a single tow of SiC fibers (Hi-Nicalon Type-S) coated with BN and embedded within a matrix of SiC formed by CVI.
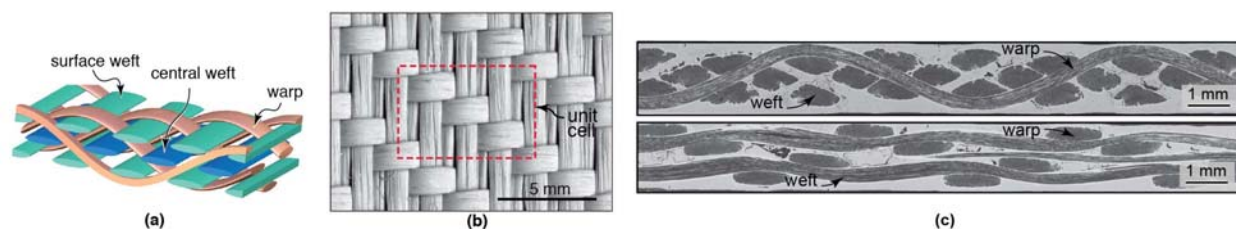
Fig. 1.2. (a) Angle interlock weave structure. (b) Partly processed composite consisting of woven carbon fiber preform coated with pyrolytic carbon and CVI SiC. (c) Fully processed composite formed by infiltrating polymer-derived SiC into the regions between fiber tows in (b).

2.2 Virtual Test and Experimental Methods

A Virtual Test system has been developed for high temperature ceramic matrix composites with stochastic textile reinforcement. While focusing in this program on ceramic composites, the formulation more generally addresses most of the challenges that can be expected when dealing with other classes of fiber composites; transition into practice is expected for both polymer and ceramic matrix composites.

The virtual tests combine experiments and theory to address physical, mathematical, and engineering aspects of material definition and failure prediction. The main research steps were: high resolution three-dimensional (3D) imaging of the microstructure, statistical characterization of the microstructure, formulation of a probabilistic generator for creating virtual specimens that replicate the measured statistics, creation of a computational model for a virtual specimen that allows general representation of discrete damage events, calibration of the model using high temperature tests, simulation of failure, and model validation.

During the course of the NHSC program, tools were developed to achieve each of these steps and the elements of the virtual test were applied to the C-SiC composite described above. Key new experiments included digital surface image correlation and µm-resolution 3D imaging of the microstructure and evolving damage, both executed at temperatures exceeding 1500°C. Conceptual advances included using both geometry and topology to characterize stochastic microstructures. Computational methods included new probabilistic algorithms for generating stochastic virtual specimens and a new Augmented Finite Element Method (A-FEM) that yields extreme efficiency in dealing with arbitrary cracking in such heterogeneous materials. The challenge of predicting the probability of an extreme failure event for a given stochastic microstructure in a computationally tractable manner, while retaining necessary physical details in models, was explored.

By necessity, developing a virtual test system requires the cooperation of researchers from different disciplines and institutions. Organizing that cooperation to generate a virtual test system that can be sustained and built upon in the future was a major challenge undertaken in the NHSC-MS program. The approach was to seek effective cooperation of different researchers by organizing research along a "pipeline" model, identifying the contributions from disciplines as sequential steps in an overall process, as indicated in the right column of Fig. 1.1. The topics constituting the virtual test system will be covered in separate sections in the following. An overview of the integrated system can be found in a recent review article [C18].

Microstructural imaging and characterization: High resolution three-dimensional (3D) imaging of the microstructures of CMCs by synchrotron x-ray tomography was undertaken at the Advance Light Source (ALS) at the Lawrence Berkeley Laboratories (LBL), in a collaboration between U.C. Berkeley (UCB) and TSC. The imaging, aimed at characterizing the 3-D fiber architecture, covered multiple size scales, from the scale of individual fibers within fiber tows to dimensions comparable to the size of the unit cell of the weave structure. Methods were developed for extracting statistical descriptions of the fiber architecture from the 3-D images, from which stochastic virtual specimens from the same statistical distribution can be generated.

For characterization of longer range defects and variability in fiber architecture, a new methodology was developed in a collaboration between UCSB and TSC, based on optical surface imaging techniques. In this approach, measured positions of characteristic surface features of the weave structure in either topographic maps obtained via 3-D digital image correlation or in high resolution scanned images, are used to generate maps of deviations from ideal positions in a perfectly regular weave structure. Analysis of these maps yields statistical parameters that can be used for virtual specimen generation.

Constitutive laws and damage development: A revolutionary new ultrahigh temperature tensile testing instrument was developed for use with *in situ* synchrotron x-ray micro-tomography, in a collaboration between UCB, TSC and LBNL. The instrument allows direct imaging of damage developing in the interior of test materials under mechanical load at temperatures as high as 2300°C in controlled environments (vacuum or controlled gas flow). It thereby provides a unique capability to calibrate material constitutive laws as one step in the virtual test pipeline. The instrument was used for imaging cracking in the fibers, matrix and interfaces of unidirectional SiC-SiC minicomposites and in C-SiC textile composites under monotonic and cyclic loading in inert and oxidative environments.

| (a) | (b) | (c) |
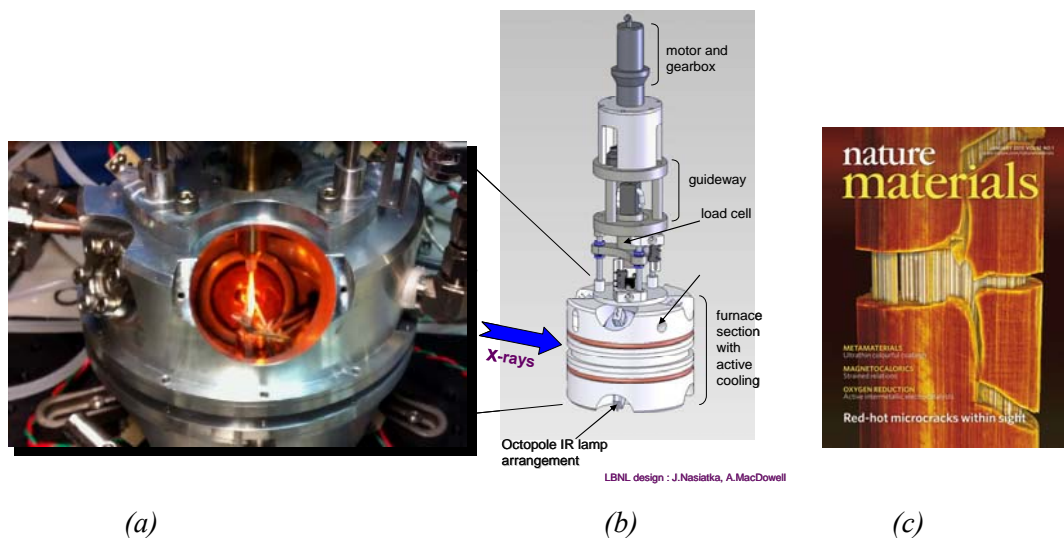
Fig. 1.3. (a,b) Test fixture for in situ synchrotron x-ray micro-tomography. (c) Image of matrix crack bridged by intact fibers in unidirectional SiC-SiC minicomposite (from cover of Nature Materials).

Specimens that can be tested in the synchrotron loading fixture with micro-tomography imaging are limited in size, to a cross section of a few mm diameter. For measuring damage development over larger size scales, the group at UCSB explored the use of digital image correlation to detect

damage by mapping surface strains during loading. They developed methods to use the technique at temperatures up to 1,500°C and used it successfully to measure thermal constitutive properties of the C-SiC textile composite and to measure the evolution of cracking in C-SiC textile composites with controlled defects in their reinforcement architecture.

Numerical methods for discrete damage: The group at the University of Miami (UM) made dramatic advances in the efficiency and capability of numerical methods for predicting multiple interacting damage modes in composite materials such as textile CMCs with complex microstructures. Using an augmented finite element method (A-FEM) that allows repeated augmentation of an element, they are now able to predict the growth of cracks that merge or bifurcate. Moreover, by avoiding the need for additional nodes or degrees-of-freedom and developing a clever algorithm that solves non-linear equations analytically at the element level, they have been able to improve the numerical efficiency be several orders of magnitude. The development of efficient fast codes is critical for the feasibility of using Monte Carlo predictions for large numbers of virtual test specimens to determine the variance of composite properties due to variability in microstructure.

Damage prediction: In collaborations between UM, UCSB, UCB and TSC, the predictions of the A-FEM method were compared with experimental observations to complete a pass through the virtual test pipeline. The statistical descriptions of the fiber architecture obtained from tomography images of a partially processed C-SiC composite were fed through the geometry generator to create the numerical model of the structure and thence to the creation of a computational mesh. This was then combined with constitutive relations (cohesive zone laws) estimated from prior experiments and the A-FEM was used to predict the evolving pattern of cracking with increasing tensile load parallel to the warp fiber tows. The predictions were then compared with DIC observations of evolving crack patterns in test specimens produced by infiltrating a full matrix into the same partially processed C-SiC composite used for construction of the virtual test specimens. The key features of the observed cracking pattern were replicated in the A-FEM analysis.

2. Background: System-Level Motivation and Rationale for Research Directions

Sustained hypersonic flight at high Mach numbers imposes a range of high heat fluxes and heat loads that vary with position on the vehicle from those that can be sustained by current materials to those that cannot, even for brief times. For the latter, designs depend on cooling by radiation or flowing fuel, or in a few locations the use of heat pipes. The ability of the system designer to close a vehicle design depends strongly on where on the vehicle it is necessary to use cooling, the efficiency of the cooling strategy, and the weight and thermomechanical performance of all the materials used, whether cooled or uncooled. The National Hypersonic Foundational Research Plan and other high-level studies[1] leading up to the beginning of the NHSC programs in 2009 had identified materials and structures capable of surviving high temperatures as critical technologies and major drivers of development risk and operational success for hypersonic flight.

Specific deficiencies in existing materials depend on the location on the vehicle as well as the operating mission, Mach number, and lifetime. Some of the most severe materials challenges are embodied in two examples:

1) Leading edges (nose, cowl lip, and control surfaces) are exposed to extremely high heat fluxes on small tip regions that are difficult to access for active cooling (preferred designs for low drag may have tip radius smaller than 1 mm and wedge angle less than 10°, leading to surface temperatures over 2200^oC). Without active cooling, the only apparent solutions are materials with combined high temperature capability and high thermal conductivity (to spread the heat for dissipation by radiation or conduction to a heat sink). As illustrated in the property map in Fig. 2.1b, the major contenders for materials that fill this need are refractory carbides and borides or C-C composites with aligned high conductivity fibers. However, all these materials are limited in application by their susceptibility to severe oxidation, as well as cracking induced by high thermal gradients. Advancing the science needed to overcome these limitations was one of the research goals of this program. This included understanding oxidation mechanisms and devising new approaches for improving the stability and life of refractory diboride materials at high temperatures.

2) In the propulsion flow path, where radiation cooling is not available, active cooling using the fuel (hydrogen or hydrocarbon) is essential. For sustained flight at high Mach numbers, the system design requires a material with high strength-to-weight ratio (since the structures forming the propulsion flowpath have large area) and capable of operating with high surface temperatures to minimize heat absorbed and thus the fuel required for cooling. [2] Ceramic matrix composites (CMCs) (and carbon-carbon composites) are the only classes of materials so far identified as potentially capable of satisfying these requirements: as illustrated in Fig. 2.1c, the specific strengths of CMCs (C-SiC and SiC-SiC) and carbon-carbon at temperatures above about 1200^oC exceed those of competing refractory metals by about a factor of three. Thin skins are required with complex geometrical features, including internal channels for coolant flow (either regenerative or transpiration cooling) and features to allow attachment to the surrounding

---

[1] (a) Report to Congress: Roadmap for Hypersonics Programs of the Department of Defense, Joint Technology Office on Hypersonics, February 2008

(b)Hypersonics Technology Status and Development Roadmap, AIAA HyTASP Prog. Comm., K.G Bowcutt (2003)

structure. Advances in textile-based CMCs have established a capability for forming integral structures with 3-D reinforcement architectures that have been shown to satisfy the demands of a wide range of severe thermo-mechanical environments.[2] However, the application of these materials is held back by several shortcomings: (i) surface temperatures remain limited to the range ~1,400°C – 1,600°C, whereas higher temperature capability is desirable for durability, especially in regions susceptible to heat spikes from shock interactions or combustion instabilities; (ii) lifetimes are limited by oxidation, which is exacerbated by microcracking driven by high thermal gradients, especially at the highest use temperatures; and (iii) a capability for high-fidelity modeling of damage and lifetime does not exist. The need for high-fidelity modeling capability is especially critical for textile composites, where the fiber architecture and hence the composite properties vary from place-to-place in a component making standard data bases of material properties insufficient for design or life prediction. The development of tools capable of overcoming these limitations under the umbrella of a virtual test system that integrates contributions from researchers in different disciplines and institutions was one of the goals of the NHSC-MS program.
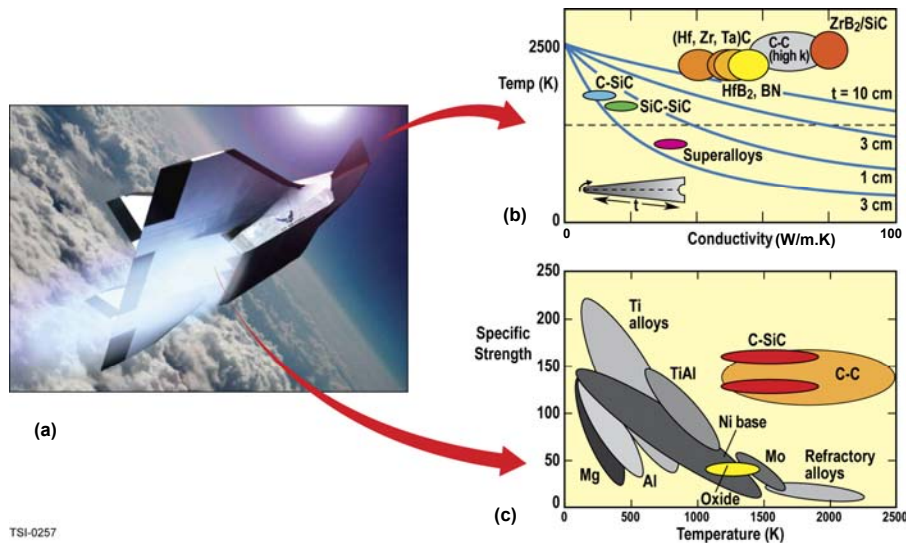

Fig. 2.1. (a) Visualization of hypersonic vehicle. (b, c) Material property comparisons for leading edges (b) and large-area hot structures (c).

---

[2] D. B. Marshall and B. Cox, "Integral Textile Ceramic Structures," Annu. Rev. Mater. Res., 38 425-43 (2008)

3. Virtual Test

Variability in the spatial deployment of fibers (geometrical defects in the textile) contributes to variance in the properties of their composites. In the virtual test development, the stochastic characteristics of the fiber positions were determined experimentally at all relevant scales and summarized in standard, simple datasets. These datasets become the input for the next step: the process of constructing virtual specimens that possess stochastic microstructures with the same statistics.

Details of the characterization of stochastic data for fiber positioning are as follows.

3.1 Stochastic Characterization at the Tow and Sub-Component Scales

In nominally periodic textiles, the positions and shapes of tows can be expressed as the sum of non-stochastic, periodic variations associated with the nominal periodicity of the textile architecture and stochastic deviations from these average trends, which vary randomly through the fabric. A convenient and intuitively appealing treatment of the deviation divides it in turn into a superposition of "short-range" and "long-range" deviations. The short-range deviations, determined by μCT, are those arising within a unit cell and include variations in the shapes of tows as well as their positions. We refer to this as the "tow scale". The long-range deviations, determined from optical surface images, are the displacements of tows over wavelengths that are greater than the unit cell, comparable to a sub-component (dimensions typically of order of magnitude 100 mm). We refer to this as the "sub-component scale". At even higher spatial resolution than the tow scale, data can be analyzed for fibers that are present as discrete entities. We refer to this as the "fiber scale".

A common characteristic of analyses at the three scales (fiber, tow, and sub-component) is that, in the direction along any tow, spatial variations in stochastic deviations of any positional or shape characteristics vary relatively slowly; the continuity of the fibers has a mechanical smoothing effect on geometry variations. Therefore, at all scales, variations along the fiber direction can be analyzed using relatively simple methods with few degrees of freedom in fitting parameters.

At the tow scale, periodic trends were compiled by exploiting the nominal translational invariance of the textile: data from all points on nominally equivalent tows throughout the specimen were collated onto a single periodic cycle of that type of tow, a process called "reference period collation" [C6,C7]. This process maximizes the information content of relatively small specimens imaged at high resolution. The stochastic deviations from the periodic trends consist of the set of standard deviations of the cross-sectional characteristics. For the materials studied, the deviations were found to be independent of location along the tow.

At the sub-component scale, long-range deviations were determined as displacements of entire tows from the locations expected for a perfectly periodic ideal. Details of their treatment are presented below.

At the tow scale, geometrical details of the fiber reinforcement were determined using μCT, as described above. Typical 2D image slices of a 3D woven C/SiC composite are shown in

Fig. 3.1a, along with a 3D image of a unit cell in Fig. 3.1b. This material was fabricated with only enough matrix to rigidify the structure, which simplified identifying tow domains [C6].

For the shapes typical of tow cross-sections in textiles, statistical analysis of the shape and positioning of the fiber tows can be based on analysis of sequences of cross-sections along the tow axis. For the convex or mildly re-entrant cross-sectional shapes typical of tows, moment expansions of the shape function $\Omega(y, z)$ are a good general description:

$$\omega_{pq} = \iint y^p z^q \Omega(y,z) dy dz \tag{1a}$$

$$\Omega(y,z) = \begin{cases} 1 & \text{if } (y,z) \text{ lies inside the tow} \\ 0 & \text{if } (y,z) \text{ lies outside the tow} \end{cases} \tag{1b}$$

where the nominal tow direction is the *x*-axis and *p* and *q* are integers (the moment orders). In cases where tow cross-sections are free of re-entrant features, a serviceable truncation of the moment expansion can be obtained by fitting ellipses to data (even though the cross-sections may deviate from elliptical). A fitted ellipse defines five of the six moments of order $o = p + q \leq 2$, with the sixth moment having a fixed relation to the other five, because of the particular shape of the ellipse. Ellipse fitting yields the data set:

$$\{ y^{(m)}, z^{(m)}, A^{(m)}, ar^{(m)}, \theta^{(m)} \} \tag{2}$$

where $y^{(m)}$ and $z^{(m)}$ are the center-of-mass coordinates and $A^{(m)}$, $ar^{(m)}$, and $\theta^{(m)}$ are the area, aspect ratio, and orientation, respectively, of section *m*, one of a sequence of cross-sections on a discrete grid. In cases where cross-sections possess highly distorted shapes, such as strongly re-entrant features, characterization should be based on higher order moment expansions or other generalized shape descriptors.

For a textile that is nominally periodic, each variable in Eq. (2) can be decomposed into non-stochastic, periodic variations and non-periodic, stochastic variations [C6,C7]:

$$(y,z)^{(m)} = \left\langle (y,z)^{(m)} \right\rangle + (\delta y, \delta z)^{(m)} \tag{3a}$$

$$A^{(m)} = \left\langle A^{(m)} \right\rangle + \delta A^{(m)} \tag{3b}$$

$$ar^{(m)} = \left\langle ar^{(m)} \right\rangle + \delta ar^{(m)} \tag{3c}$$

$$\theta^{(m)} = \left\langle \theta^{(m)} \right\rangle + \delta \theta^{(m)} \tag{3d}$$
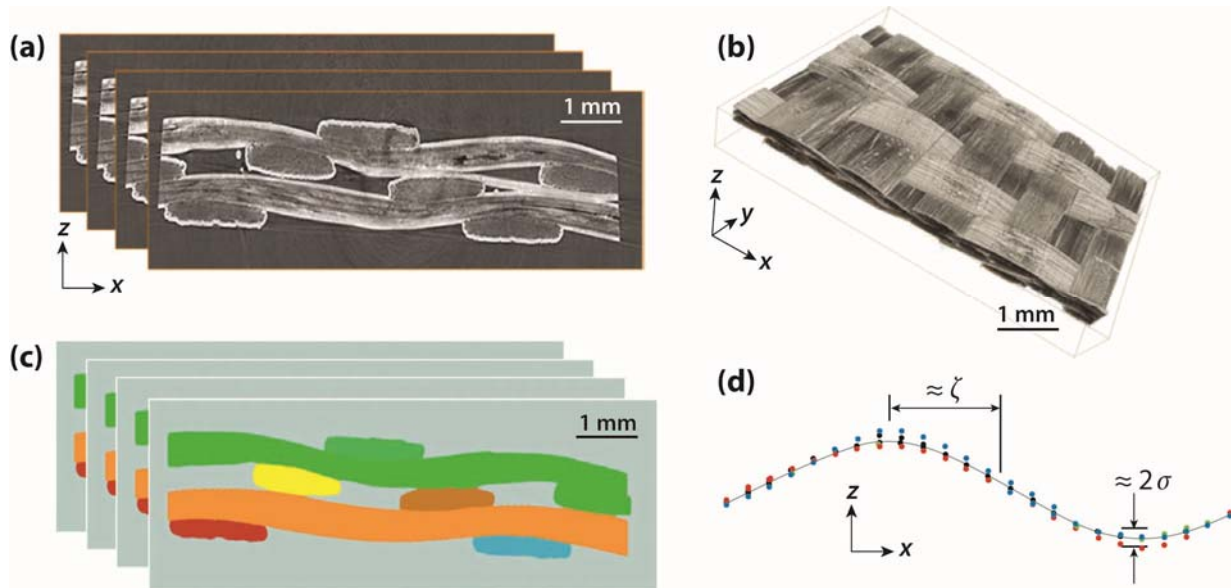
where $\langle .. \rangle$ indicates an average value.

Figure 3.1. Analysis of μCT data for a carbon/SiC woven composite, consisting of fiber tows coated by a thin layer of matrix material. (a) Image slices. (b) Re-constructed 3D image. (c) Segmentation of image into tow domains. (d) Inferred statistics for the z-coordinate of the warp tow locus: curve shows average trend for warp tow over one reference period (which spans one unit cell of the textile architecture), while blue, red, and black dots show data for different warp tow segments. The deviations of data from the mean have RMSD σ, while the distance along the tow over which deviations are correlated defines the correlation length ζ..

The periodic trends are compiled by the process of reference period collation. The stochastic deviations from the periodic trends consist of the set of standard deviations, $\sigma_y^{(k)}$, etc., of the cross-sectional characteristics. The superscript k denotes a tow genus, i.e., a set of warp or weft tows that are nominally equivalent to one another in the periodic pattern of the weave. Another statistic of interest is the correlation length $\zeta_y^{(k)}$ for each cross-sectional characteristic, which measures the distance along the tow over which correlations between the values of deviations at two points become weak. For the materials of Fig. 3.1, the deviations are found to be independent of location x along the tow.

After analysis has determined the important statistical variables for a given data set, the stochastic character of the tow positions and shapes can be summarized by a specific, quite small set of statistical variables. The set comprises the deterministic variations of each tow over a single period, defined on a grid of typically 20 points, and ten other scalar parameters that contain all information about stochastic variations at the unit-cell scale. These descriptors completely define the 3D shapes of tows and the statistics of their shape deviations. Crucially, they provide a standard protocol for passing information from experiment into a virtual specimen generator and thence into analyses of how stochastic microstructure at the unit-cell scale affects performance.

Details of the treatment of stochastic deviations in the geometry of textiles at the tow and sub-component scales can be found in [C6-10,C19,D9]. A significant contribution to this study was a collaboration with the Katholiek Universitet de Leuven, Belgium, which applied and extended

the analytical methods developed in the NHSC using data for polymer composites, with different textile architecture, at the tow and sub-component scales.

3.2   StochasticCharacterization at the Fiber Scale

Characterization at the fiber scale focused on quantifying the degree of entanglement of meandering fibers in a random bundle. Data were again acquired from synchrotron-based X-ray computed tomography; these data provide complete descriptions of the stochastic positions of each fiber in large bundles within composite samples. The data were accumulated for distances along the nominal fiber direction that were long enough to reveal meandering or misalignment of individual fibers. Data were analyzed for a single fiber bundle consolidated as a mini-composite specimen and a block of fibers embedded within a single ply in a tape laminate specimen. The fibers in these different materials differ markedly in their departure from alignment and the patterns formed by fiber deviations.

A combination of topological and Euclidean metrics to characterize bundle properties in these and other materials was proposed. Topological metrics are based on the neighbor map of fibers, which is constructed on cross-sections of the bundle by Delaunay triangulation (or Voronoi tessellation). Variations of the neighbor map along the fiber direction describe fiber meandering, twist, etc. Euclidean metrics include local fiber packing density and fiber orientation. Both topological and Euclidean metrics are stochastic. They are expected to influence both the mean and variance of composite properties, especially fracture strength, toughness, and fatigue life.

One key topological metric is the rate at which the set of fibers constituting the nearest neighbors of a given fiber varies along its length. For a given fiber length, a related metric is the total "map change count" n_{mc} for each fiber. Also of interest is how this metric is correlated among fibers that are neighbors (Fig. 3.2a), which determines the degree to which fibers with unusually tortuous loci appear in clusters within the bundle. A key Euclidean metric is the spatial distribution of the local volume fraction, which can be determined for individual fibers from the area of the Voronoi polygon associated with that fiber in the random bundle (Fig. 3.2b).

The metrics provide databases that distinguish bundle types, enable quantification of the effects of the manufacturing history of bundles, and provide target statistics to be matched by virtual specimens that might be generated for use in fiber-scale virtual tests. Matching the set of Euclidean metrics assures that a virtual specimen has the same spatial distribution of fibers on any cross-section. Matching the set of topological metrics assures that the fiber meandering is correctly matched.

Details of analysis at the fiber scale can be found in [C22]. This research topic was augmented by a collaboration with the University of Southampton, UK, especially the data acquired by Dr. Anna Scott for polymer composite tape laminates using the European synchrotron facility in Grenoble.
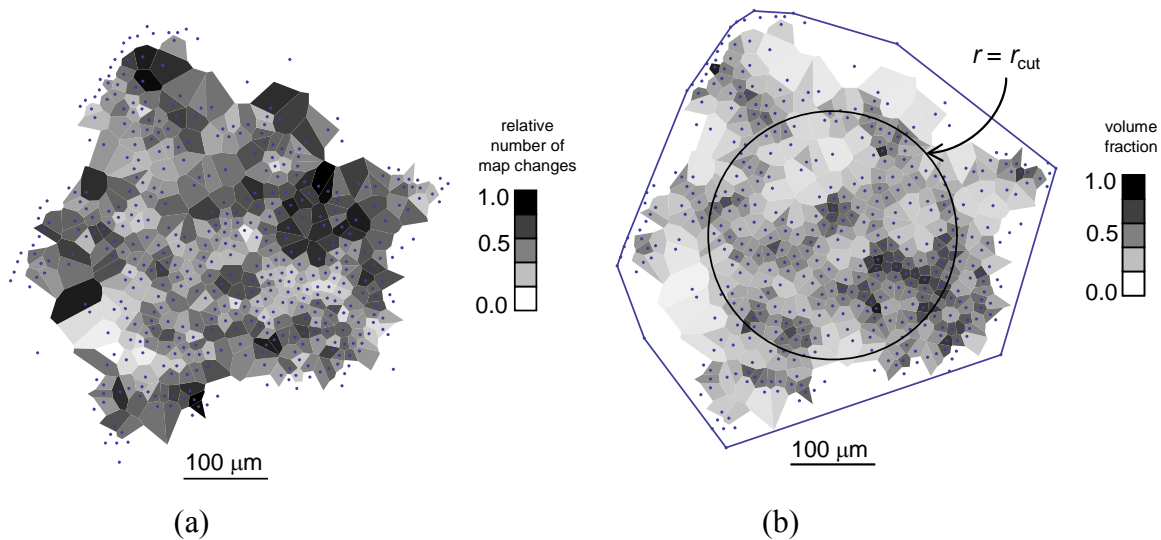
Figure 3.2. Single-tow specimen. (a) Voronoi polygons determined on one cross-sectional plane. The gray-scale of each polygon indicates the relative map change count n_{mc} along each fiber. (b) Gray-scale indicating the value of v_f determined at that fiber.

3.3 Generating Stochastic Virtual Specimens

The next step in assembling a virtual test is to formulate a reconstruction algorithm or generator that creates stochastic virtual specimens whose statistics match those of the image data. A successful generator must match the target experimental statistics; such data sets calibrate the desired generator.

In this study, tow shapes and their deviations at the tow scale were generated using the standard set of statistics described above. The simplest generator exploits the linear continuity of tows in the textile: a Markov Chain algorithm generates fluctuations in any tow cross-sectional characteristic by marching systematically along the tow's length [C8]. The key element of the Markov Chain is the Probability Transition Matrix (PTM), which determines the deviation of any characteristic at any point on the tow given the deviation at a prior point. Whether the two deviations are strongly or weakly correlated depends on how the separation of the points compares to the correlation length for that characteristic.

The Markov Chain algorithm is implemented within a Monte Carlo scheme. An instantiation μ_1 of any deviant quantity μ at the first grid point on a tow is determined by choosing a uniform random number and then passing that number through a re-scaling operation that maps it onto the prescribed distribution of μ. Given μ_1, a second random number is chosen and rescaled through the PTM of the Markov Chain to generate the value μ_2 for the second grid point. The latter step is repeated along the entire tow. Details of the implementation appear in [C7,C8].

Virtual specimens with 1D representations of the textile reinforcement can be generated by applying the Markov Chain algorithm to the tow center-of-mass coordinates only, ignoring the other characteristics of tow cross-sections related to their area, etc. The resulting 1D tow models

(Fig. 3.3) can be incorporated into the Binary Model for analysing the mechanics of textile composites, by combining them with solid 3D elements that create the external shape of the composite and carry constitutive properties representative of the composite matrix [C7,C8]. The Binary Model is the lowest order computational representation that retains the interlacing pattern of the discrete tows in a textile. When analyzed in conjunction with gauge-averaging methods, i.e., averaging predicted strains over gauge lengths comparable to a tow width, mesh-independent predictions of local strain variations are obtained. The predictions correlate well with strength data for textiles in cases where failure does not involve significant damage progression (i.e., where failure is quasi-brittle). Extension to ceramic matrix composites with highly nonlinear matrix response has also been demonstrated.
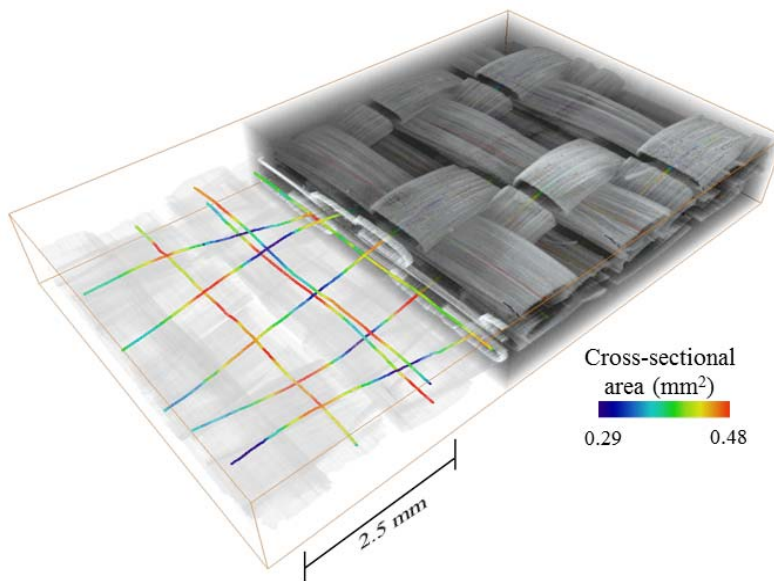

Figure 3.3. A μCT image yields statistics that are matched by generated virtual specimens. In this schematic, the generated tow structure at the left of the collage represents tows by 1D loci, suitable for use in the Binary Model.

Virtual specimen generators with 3D tow representations have also been developed. This is done by using the Markov chain algorithm described above to generate stochastic tow shapes, e.g., area, aspect ratio, and orientation of successive cross-sections of the tow. When this is done, interpenetration errors can arise, which have been a universal headache in the generation of complex textile models. Prior methods that have achieved greatest realism used mechanics-based algorithms, combining deformation simulations with methods of tracking the contact surfaces between tows. The difficult nonlinear problem of tracking contact surfaces has been approached by either geometrical contact models, which can be very complex, simplified rules combined with FEM computations, or deformation computations acting alone.

An alternative method, which is failsafe and computationally rapid, invokes the topological ordering rules that define the textile architecture (C9). For each pair of tows, the rules prescribe which tow should lie under or over the other, if the tows are orthogonal; or which should lie to the right or left, if they are nominally parallel. The topological rules correct errors without ambiguity. Topological algebras appeared in textile science a quarter of a century ago and have

recently become a key part of generating textile models. Correcting ordering errors during virtual specimen generation by invoking formally tabulated topological ordering rules leads to very robust methods that can deal with arbitrary errors. Illustrations have appeared for virtual specimens of arbitrary size with stochastic tow shape variations, as well as models of non-stochastic single unit cells with periodic boundary conditions.

The generation of virtual specimens at the sub-component scale is described in Section 5. The generation of fiber-scale virtual specimens remains a topic for future study.

3.4 Future Pathways Exploiting Virtual Specimens

Stochastic virtual specimens, i.e., formulations for generating instantiations of stochastic fiber deployment at the fiber, tow, and sub-component scales, have two primary uses: in simulations of composite processing and simulations of the failure of the finished composite product. Details of failure predictions based on stochastic virtual specimens appear below. Some thoughts on the application of stochastic virtual specimens in simulations of processing have been communicated to investigators at AFRL, who are planning a new program on the topic. Key research targets include the prediction of defect populations in processed CMCs, including voids and initial microcrack populations, relation of such populations to variability in fiber positioning, and mitigation of the defects by the optimization of processing cycles.

3.5 Computational Mesh

For applications of virtual specimens involving the prediction of progressive damage, especially in a discrete-crack representation such as the A-FEM described below, the conversion of the virtual specimen defined as a 3D geometrical entity into a computational mesh is non-trivial. At the tow scale, the 3D tow shapes must be meshed by elements that satisfy a number of conditions necessary for effective implementation of the A-FEM: shapes must be represented by tetrahedral elements and the facets of the tetrahedra that constitute the surface of different material domains that are in contact must be identical over the contact region. This latter condition has proven challenging: it is not easy to identify domains of contact and then define tetrahedra in different material domains that have desirable shape and size characteristics and are identical within the contact domains. Furthermore, great incentive exists for developing meshing strategies that minimize the number of elements used and still lead to high-fidelity simulations of damage evolution.

While many calculations of composite behavior using non-ideal computational meshes have been performed (reported below), two approaches to achieving an optimized mesh are being pursued in ongoing work. One is to begin with continuous representations of the 3D geometry of a tow, represented by tetrahedra that have no constraint on their shapes and sizes, and proceed to satisfy the condition of compatibility at contact domains and minimize the total elements used. The second is to begin with a voxel representation of the tow shapes, i.e., using elements constrained to be cuboidal in shape and uniform in size, and use the ability of the A-FEM to introduce material discontinuities within an element to re-introduce the 3D detail of curved tows in the computational formulation.

These two approaches are radically different strategies and both are novel contributions to the literature on textile representations.

4. Synchrotron X-Ray µCT for *In Situ* Imaging of CMCs at High Temperature

Characterizing and modeling the evolution of damage and failure in textile ceramic matrix composites are crucial for their design, optimization and life prediction. Owing to their complex structural architectures, these materials must be characterized in three dimensions (3-D), ideally under load at representative temperatures (≥1500°C). Currently, this can be achieved using serial sectioning following the interruption of mechanical tests, involving the cooling of the sample with likely changes in the stress states and resulting cracking patterns. Virtual testing offers the possibility of probing details of damage mechanisms for different temperature and loading histories by using simulations. However, to be effective such simulations must be coupled to realistic characterization and quantification of the salient physical mechanisms. The proven fidelity of a virtual test can never exceed the ability to identify the mechanisms that must be modeled by direct experimentation.

The main purpose of the work summarized in this section was to harness the non-destructive, high-resolution imaging capability of x-ray synchrotron computed micro-tomography (µCT) at the Advanced Light Source (ALS), Berkeley, CA, to characterize the 3-D geometric microstructure of woven textile composites and quantitatively characterize the mechanical and environmental damage mechanisms and microscale failure events in these materials under tensile loading at temperatures up to 1750°C or more.

The experiments were focused on the C-SiC and SiC-SiC composite materials described in Section 1.1.

4.1 3D Structural Characterization of Woven Textile Composites

Initial studies focused on generating µ-CT images of C-SiC and SiC composites with the best possible contrast and resolution, including the critical task of tuning the setup to minimize scan times without compromising image quality. Three-dimensional µ-CT images were obtained demonstrating sub-micron resolution with sufficient contrast to distinguish microstructural features of interest: carbon fiber tows in SiC matrix; individual SiC fibers and BN coatings within a fiber tow in a SiC-SiC composite; SiC fiber tows within a SiC matrix; and regions of SiC matrix formed by different routes that result in small differences in density (chemical vapor deposition versus polymer infiltration and pyrolysis). The ability to distinguish small differences in SiC matrix density enables monitoring of microstructural development during material processing.

To generate the 3-D images such as Figs. 3.1 and 3.3, used for extracting statistical descriptions of the fiber architecture in the Virtual Test, partially infiltrated C-SiC composite test specimens as shown in Fig. 1.2b were imaged. Then, through a series of image segmentation and shape fitting operations, the complete 3D spatial coordinates of individual tows in a three-layer angle interlock textile composite were determined. Following the protocols detailed in Section 3, the data were then represented by a relatively small number of characteristics, namely the tow centroids and the area, aspect ratio, and orientation of the tow cross sections at each position along the tows as illustrated in Fig. 3.3. Variations in these characteristics along the tows were then measured and used to calculate deviations from non-stochastic periodic geometrical characteristics.

4.2. Development of an *in situ* Rig for Ultrahigh Temperature Material Characterization

A high temperature loading stage was designed and constucted for *in situ* x-ray micro-tomography using synchrotron radiation at the Advanced Light Source (ALS), Lawrence Berkeley National Laboratory (LBNL). The rig allows for real-time imaging of test materials under mechanical load at temperatures up to 2300°C in controlled environments (vacuum or controlled gas flow). Sample heating is achieved by six infrared halogen lamps with ellipsoidal reflectors arranged in a confocal configuration, which generates an approximately spherical zone of high heat flux approximately 5 mm in diameter. Samples held between grips connected to a motorized stage are loaded in tension or compression with forces up to 2.2 kN. A robust pyrometer system was implemented that allows continuous measurement of the specimen temperature to within ±20°C while running tomography scans. Experiments confirmed that the instrument is capable of operating with specimen temperatures above 2000°C in flowing gas environments (either inert or active). More recent upgrades to the system include fully programmable load and temperature cycles including electronic flow control and switching of different gases into the environment chamber while in situ experiments are running.

The entire instrument is mounted on a rotation stage that allows stepwise recording of radiographs over an angular range of 180 degrees. A thin circumferential (360 degree) aluminum window in the wall of the heating chamber allows the x-rays to pass through the chamber and the sample over the full angular range. Scan times have recently been reduced to several minutes without loss of image quality through the use of a high-frame-rate camera and an improved high-efficiency scintillator. Even shorter scan times can be achieved at the expense of image quality by limiting the number of radiographs collected in each scan. These advances in synchrotron facilities show promise for enabling *in situ* tomography under near-continuous loading conditions.

4.3. Observations of Initiation and Growth of Internal Damage in Ceramic Matrix Composites above 1700°C

Examples of the damage observable during *in situ* loading experiments with two different composites are shown in Fig. 4.1. In the case of a unidirectional SiC/SiC composite tested at room temperature and at 1750°C (Fig. 4.1a), two types of damage are visible: cracks in the matrix oriented approximately normal to the applied force (and the fibers); and fractures of individual fibers at locations that do not coincide with the matrix cracks. The matrix cracks extend across the entire cross-section of the test specimen, while remaining bridged by intact fibers. The crack bridging response is responsible for the tough behavior of these composites and is enabled by the weak layer of BN surrounding the fibers, which allows debonding and frictional sliding. The locations and loads at which individual fibers fracture are dependent on the statistical distribution of flaws in the fibers and the magnitude of the frictional sliding stress. These are the key constitutive properties dictating the macroscopic stress-strain response of the composite that are needed as input for models that predict mechanical performance and lifetimes. Measurements of the opening displacements of the matrix cracks can be used to calculate the frictional sliding stress between the matrix and fibers. In this case, the frictional stress was found to be lower at room temperature than at 1750°C. The decrease in sliding resistance at high temperature has been attributed to changes in the structure of the BN layer at high temperature.

In the case of the C-SiC composite with textile reinforcement (Fig. 4.1b), subtle differences between the paths taken by evolving cracks are evident in tests at room temperature and at 1750°C.

Experiments such as these contain a large amount of quantitative information on crack paths, crack surface areas and orientations, spatial variations in the crack-opening displacements, statistics of relative spatial location of cracks and microstructural heterogeneities within the sample volume; all these parameters are critical in any analysis of fracture as they govern the toughness of the material or in a Virtual Test. Success in making use of this data rests on efficient methods for processing the 3-D image data with techniques such as segmentation for automated identification and representation of cracks and microstructural features. Presently this is a bottleneck in need of further research
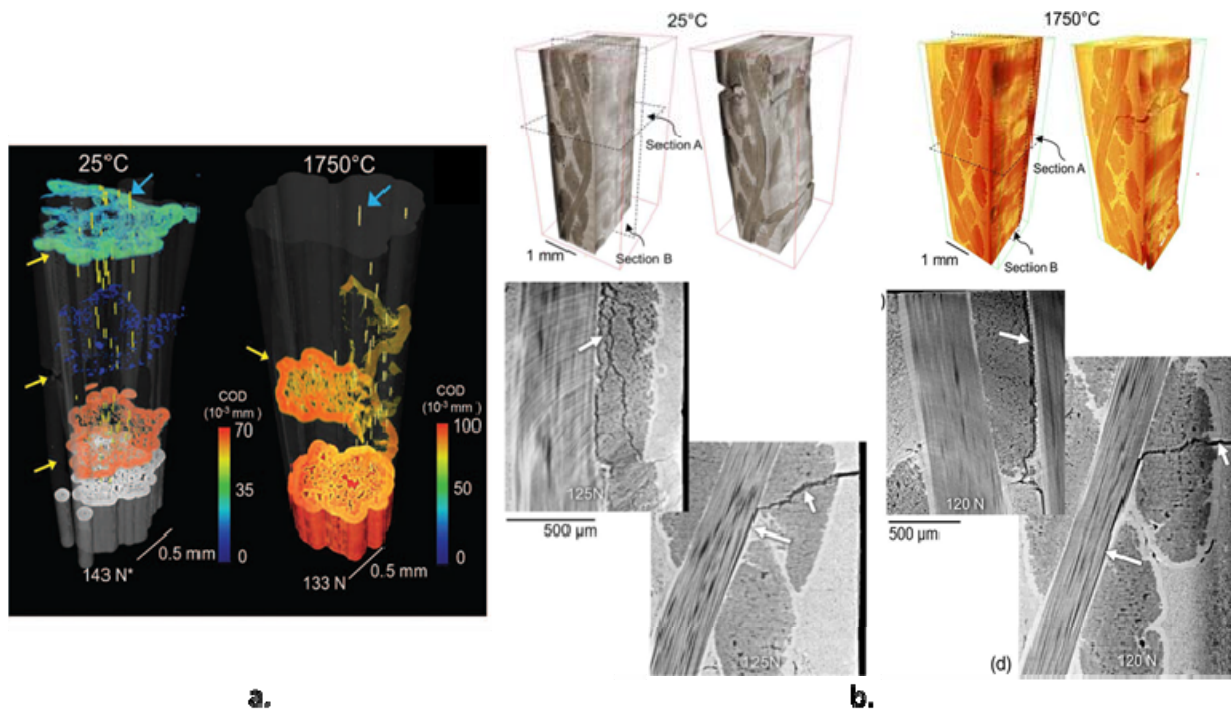

Figure 4.1: (a) 3D visualization of matrix cracks and fiber breaks for two unidirectional SiC-SiC composite specimens under tensile load at 25°C and 1750°C.(b) Internal image slices from two C-SiC specimens during testing at 25°C and 1750°C, showing cracks deflecting from transverse fiber tows to longitudinal tows.

4.4. 3D Microscale Observations of Interfacial Damage in SiC-SiC Due to Oxidation

In situ experiments with the highest available imaging resolution are capable of revealing new details of micro-scale interfacial damage caused by thermal and environmental exposure. An example is shown in Fig. 4.2 of a unidirectional SiC-SiC composite that was one of a series of tests at different temperatures in oxidizing environments. In this test, at 1545°C, annular voids were observed forming in the BN coatings around individual fibers at scattered locations along the fibers. SEM analysis from sections of the composite after *in situ* testing showed extensive cracking within the BN coatings as well as the presence of very thin silica glass layers at the interface and on fiber surfaces. Experiments at different temperatures indicated the cracking of

the coating is driven by shrinkage due to structural changes in the BN at very high temperatures. This shrinkage is responsible for the lower frictional sliding stress at high temperature, as noted in the previous section. It also potentially accelerates oxidative degradation of the composite by allowing access of oxygen along the interfacial region.
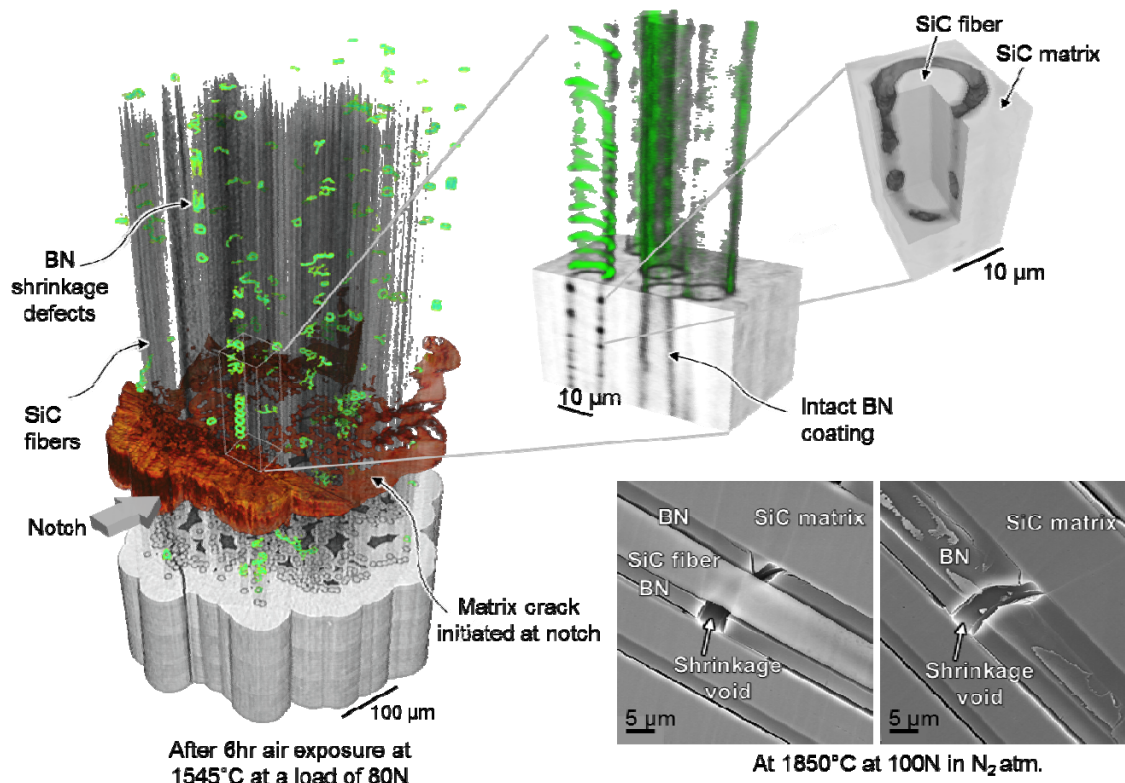

Figure 4.2: Annular shrinkage voids in the BN interface around fibers in a unidirectional SiC-SiC composite specimen at 1545°C. Left: 3-D visualization of matrix crack (brown) and fiber coating cracks(green), with matrix stripped away from image to allow internal damage to be seen). Top right:μ–CT image of fiber and coating. Lower right: post-test scanning electron microscope images.

4.4 Impact and Future Directions

The capability for high temperature testing with insitu x-ray tomography played a pivotal role in the virtual test activities the NHSC-MS program. It provided the geometrical model for the virtual test (Section 3), validation of resolution of DIC measurements (Section 5), identification of damage mechanisms, and data-rich observations of cracking for validation of AFEM calculations (Section 6). It is already impacting other (ongoing) research programs, including the following:

- *All of the major turbine engine OEMs* have initiated programs to make use of the *in situ* testing capability. The test rig has been duplicated in order to add additional capabilities.

- An *AFRL program* described in Section 6 on life modeling for SiC-SiC composites led by Teledyne (Brian Cox) is making use of the in *situ test* rig to provide constitutive properties.

- *NASA: in situ studies of lightweight carbon/phenolic ablators.* The hot-stage micro-tomography capability is being used by NASA Ames Research Center to characterize the 3-D structure of carbon fibers in a Phenolic Impregnated Carbon Ablator (PICA) and to measure ablation in situ. One of the post-doctoral fellows from the NHSC (Tony Fast) worked with NASA to analyze the tomography data to produce reconstructed tomography images and build a computational grid for numerical simulation of the ablation process. This activity is described in an AIAA paper: N. N. Mansour et al, "A New Approach To Light-Weight Ablators Analysis: From Micro-Tomography Measurements to Statistical Analysis and Modeling."

5. Test Methods and Characterization by Digital Image Correlation (DIC)

One of the program thrusts involved development and implementation of new test methods for probing the thermostructural response of ceramic composites. The objectives were threefold: (i) (i) To develop capabilities for high-fidelity strain mapping at sub-tow length scales at ambient and elevated temperature, thereby allowing calibration and assessment of virtual tests (Sections 3 and 6); (ii) To develop new protocols for identifying and quantifying sub-component scale weave defects in 3D fabrics, complementing the tow- and fiber-scale characterization via XCT at UC Berkeley (Section 4); and (iii) To formulate a phenomenological model for the inelastic response of ceramic composites at the macro-scale. Prevailing research themes include effects of matrix defects (e.g. pores and cracks) on the effective tow properties, deviations in tow trajectories from the ideal, and effects of features such as holes. Examples of such features – spanning length scales from about 1 μm to 0.1 m – are presented in Figure 5.1.
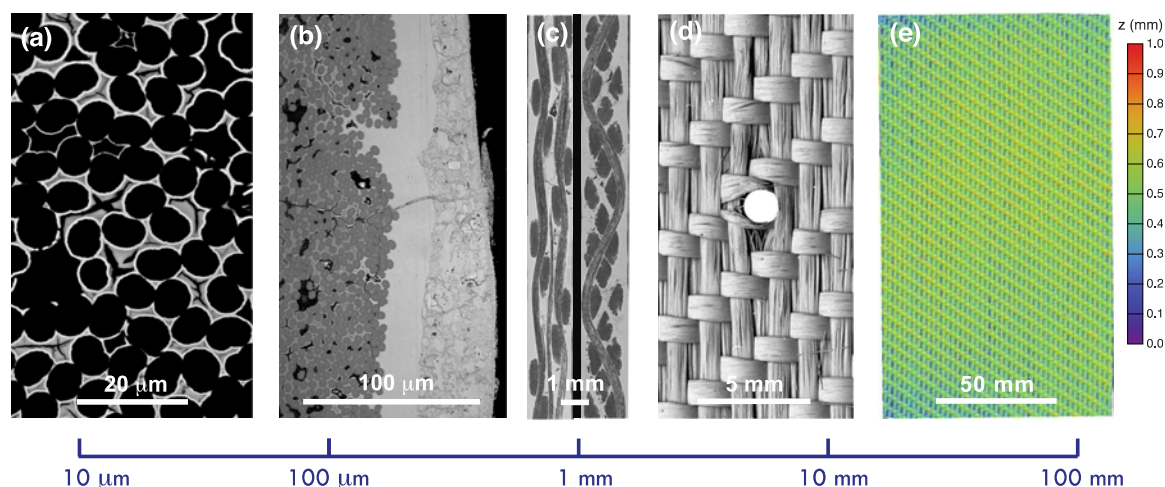

Figure 5.1: Micro- and macro-structural features of interest in woven C/SiC composites: (a) Thin CVI SiC coatings on graphite fibers and non-uniform PIP-derived SiC between fibers; (b) graded CVI SiC around tows and PIP/slurry-derived SiC, both containing cracks due to thermal expansion mismatch and/or shrinkage during pyrolysis; (c) tow shapes and trajectories over distances comparable to the unit cell dimensions; (d) small holes introduced into the fabric before matrix infiltration, and (e) long-range pattern in the woven fabric obtained by DIC.

5.1 High-Fidelity Strain Mapping

Digital image correlation (DIC) has been assessed as a tool for measuring strains with high spatial resolution in woven-fiber ceramic matrix composites [D3]. The objective was to establish a framework for design and analysis of DIC experiments that yield *high-fidelity strain measurements at sub-tow length scales*. This was accomplished by: (i) identifying and analyzing sources of displacement and strain error in mechanical tests that produce uniform strains as well as strain gradients; (ii) formulating analytic relationships between these errors and applied strain, speckle size, and DIC algorithm parameters; and (iii) utilizing the results to design experiments to probe strain variations in a ceramic composite with the requisite spatial resolution. The study yielded valuable criteria for selecting DIC test parameters to maximize the extent of correlation

and to minimize errors in displacements and strains. Importantly, the study also showed that the latter error is exacerbated by the presence of a strain gradient: a feature inherent to deformation and damage in ceramic composites. In a case study, the resulting criteria were applied to the measurement of strain fields in a 2D SiC/SiC composite. Sub-tow resolution and low strain error (ca. 10^{-4}) were achieved. The testing and analysis procedures stemming from this study have been employed extensively in subsequent investigations on C/SiC composites within the NHSC as well as numerous other research programs at UCSB.

Until recently, strain mapping at elevated temperatures (relevant to hypersonics applications) has been limited by challenges in imaging. Imaging requires use of an illumination source that can be subsequently distinguished from thermal radiation emanating from both the test specimen and the surroundings in the image recording system. Additionally, if the measurements are made in ambient air, the effects of heat haze must be mitigated. Finally, the speckle pattern must be thermally stable and provide consistent contrast over the entire temperature range of interest. Techniques that address these challenges have been developed and implemented in a laser heating facility at UCSB [D2]. They include use of: (i) high-intensity blue LEDs as the illumination source (selected because the wavelength of blue light falls outside the range of most of the black body radiation at the temperatures of interest) and corresponding blue band-pass filters on the camera lenses (to screen out all but the reflected blue light); (ii) an air knife to blow across the sample surface and mix air in the lines of sight of the imaging system, thereby reducing apparent distortions caused by heat haze; and (iii) speckle patterns created with ceramic paints that remain stable to very high temperatures. A capability for strain mapping to temperatures of 1500°C has been demonstrated.

The latter developments in high-temperature strain mapping were featured in a *Research Brief* in the *American Ceramic Society Bulletin* (**91** [5] 18-19, 2012). It also spawned interest from turbine engine OEMs, including Pratt & Whitney, Rolls-Royce and IHI Corp. Representatives from these organizations have visited the facility, with the intention of reproducing the system in their respective laboratories.

5.2. Applications of DIC to Characterization of C/SiC Composites

The preceding techniques for strain mapping at ambient and elevated temperatures have been used to probe four topics relevant to deformation and fracture of C/SiC composites: (i) weave defects introduced during the weaving operation and/or subsequent handling; (ii) anisotropic thermomechanical strains that arise upon heating; (iii) effects of woven and drilled holes on tensile properties; and (iv) effects of simulated weave defects (introduced by shear of the fiber preform before matrix infiltration) on composite properties. Highlights from each of these follow.

In-Plane Geometrical Variability of 3D C/SiC Weaves

Techniques for characterizing tow architectures and defects in woven ceramic composites are required for generating high-fidelity geometric models and subsequently probing effects of defects on composite performance. Synchrotron X-ray CT has been used to establish statistical descriptors of the shapes and positions of tows (Section 4), which, in turn, have been used to create virtual specimens with the same statistical characteristics. Despite the richness of information extracted from CT images, the technique is inherently limited to probing volumes of only about one or two unit cells of typical weaves. To address this deficiency, a new

methodology was developed for characterizing *long-range weave defects* using surface topography mapping via 3D digital image correlation (DIC). Although DIC mapping is inherently limited to characterization of external surfaces, the surfaces of composites of present interest constitute a significant fraction of all tow surfaces. Consequently, the technique provides substantial information on long-range geometric tow defects that cannot be gleaned from CT imaging alone.

Upon comparing surfaces re-constructed from CT and DIC of identical sample volumes, we have demonstrated that DIC of optical micrographs is capable of resolving surface heights with a root-mean-squared error of ~10 μm (about twice the CT voxel size, 4.4 μm) and a spatial resolution of ~20 μm over areas of many cm^2 [D7]. Achieving this level of resolution requires use of sufficiently small speckles (~50 μm) and small subset size (~300 μm) relative to the characteristic tow dimensions (~1 mm).

Having established the fidelity of surface topography mapping using DIC, the technique was employed to characterize *in-plane weave variability* in textile composites [D9]. The methodology involves: (i) determination of surface topography using high resolution image pairs and 3D image correlation; (ii) identification and segmentation of the positions of a prescribed population of surface tows for use as fiducial markers; (iii) determination of a hypothetical perfectly periodic pattern that best fits the stochastic positional data for tows; (iv) determination of in-plane deviations in the nodal positions from their positions in the hypothetical ideal and partitioning of these deviations into short- and long-range components; (v) calculation of spatial derivatives of deviations; and (vi) spectral analysis of the spatial derivatives by Discrete Fourier Transforms (DFT). The analysis yields a compact set of statistical parameters that characterize the mean and standard deviation of the amplitudes of the Fourier components as well as the correlation lengths for variations in amplitude and phase of the Fourier components. An algorithm for constructing virtual specimens with the same statistical variations consists essentially of reversing the steps outlined above. Specifically, values for the amplitude and phase of each Fourier coefficient are determined using a Monte Carlo method. The amplitude is evaluated for a sequence of scan lines using the Markov Chain algorithm, calibrated by the statistical parameters emerging from the spectral analysis of the spatial derivatives. With a complete set of complex Fourier coefficients thus established, the tow packing density variations are determined by inverse DFT and the tow positional deviations are determined from these by integration. Examples of the short-range packing density variations obtained experimentally and re-constructed computationally are presented in Fig. 5.2.
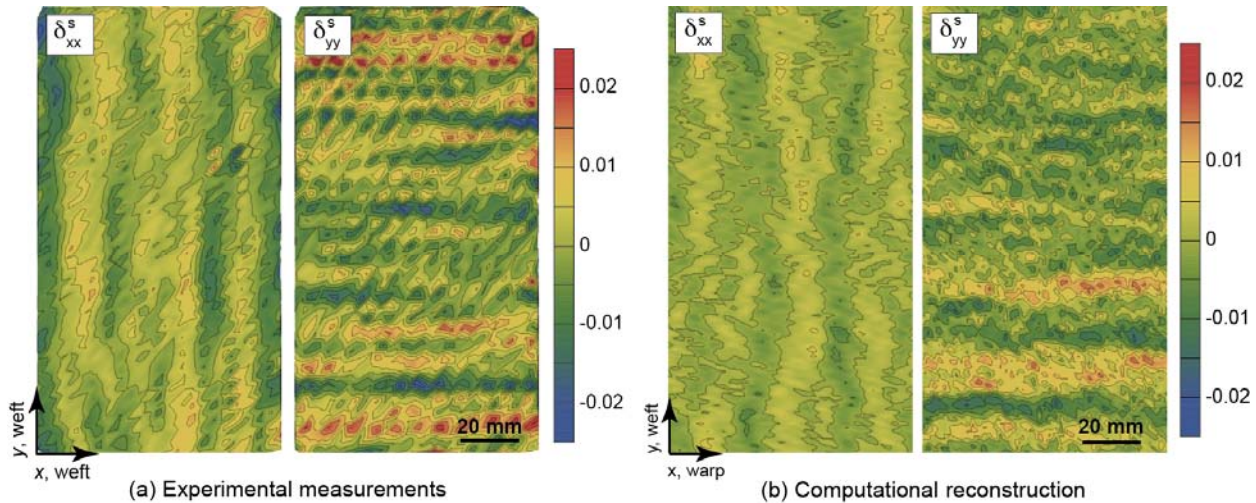
Figure 5.2: Short-range deviations in packing density of warp and weft tows obtained from experimental measurements and subsequent computational reconstruction.

Calibration of Thermoelastic Tow Properties in a Woven C/SiC Composite

A methodology has been developed for calibrating the *thermoelastic properties of constituent tows* in a woven C/SiC composite using a combination of experimental strain measurements and finite element simulations [D8]. Because of the non-uniform distribution of the matrix phase and the presence of matrix microcracks, tow properties cannot be reliably predicted *a priori* using micromechanical models alone; instead, some can only be inferred from coupled experimental/numerical studies. Experiments to measure surface strains were performed using the heating and imaging facility described above. A representative set of thermal strain maps is shown in Figs. 5.3(a) and (b). Superimposed on the maps are the approximate locations of the tow boundaries. The tows exhibit anisotropic thermal expansion. For instance, the axial strain in the weft tows is about half that in the transverse direction. Additionally, because of fine-scale intra-tow variations, *area-averaged strains* within individual tow segments are used in comparisons between experimental measurements and finite element simulations. A small number of iterations of finite element simulations is required to achieve satisfactory agreement in all thermal strain components. The number of iterations is minimized by first performing simulations using model-based estimates of the effective tow properties, followed by judicious adjustments to select property values. The study reveals that the strains within nominally-equivalent tow segments exhibit considerable variation. These variations are attributable to variations in both tow geometry and connectivity between adjacent tows. Importantly, the virtual tests predict not only the correct average strains but also the strain variations within each tow genus (Fig. 5.3(c)).
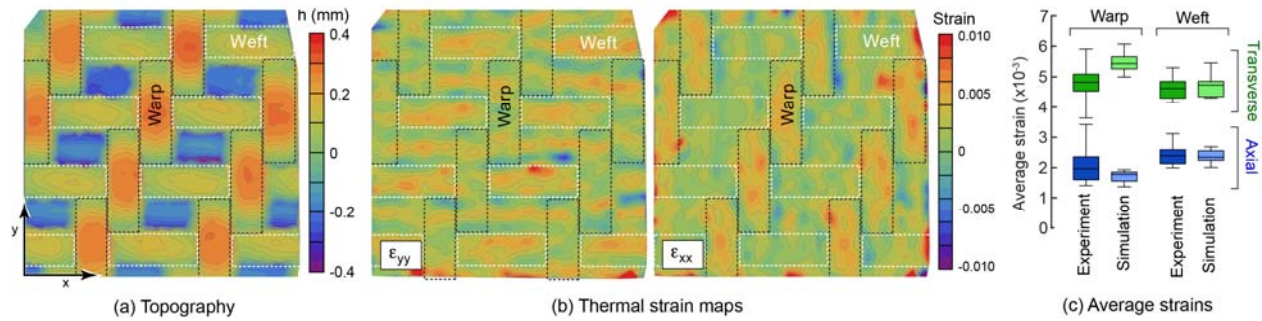
Figure 5.3: *(a) Topography and (b) thermal strain maps obtained on a C/SiC composite at about 1000°C. (c) Comparisons between measured and computed average strains in the warp and weft tow segments [D8].*

Effects of Open Holes on Tensile Properties

With the recognition that some CMC components are likely to contain features such as holes for cooling, fuel passage or attachment, a study was performed to investigate the effects of small holes on the tensile properties of a woven C/SiC composite [D10] (Figs. 5.1(a)–(d)). The holes were introduced by one of two methods: by insertion of fugitive rods into the woven preform before adding the matrix or by conventional machining after panel fabrication. The holes produced in the former manner cause negligible distortion of the surrounding weft tows and only small changes in warp tow packing density (Fig. 5.1(d)). Upon tensile loading, in both warp and weft orientations, the surface (matrix) strains are accommodated by opening of matrix cracks, initially either open or partially-filled by the PIP process. In the *weft* orientation, the stress-strain response and the failure stress are readily predicted on the basis of the fiber properties, assuming these fibers to be straight (a good approximation in this orientation). In contrast, in the *warp* orientation, the response exhibits important effects from straightening of initially wavy tows and bending stresses that, when superimposed on the axial tension, result in reductions in tensile strength and failure strain. Additionally, the tensile strength exhibits only a weak sensitivity to the presence of the holes, with woven holes being somewhat less detrimental than drilled holes. Comparisons of strain maps reveal important effects of damage at various length scales, dictated by the dimensions of the tows, the unit cell and the hole (when present). A crucial implication is that the mechanisms governing global inelastic deformation – including cracking at the tow-level and at the unit cell level coupled with the strain concentrations of the holes – are tightly intertwined and can only be extricated using the virtual test capabilities described in Section 3.

Effects of Preform Shear

Woven C-fiber preforms exhibit defects, introduced either during the weaving operation or during subsequent handling. In an effort to identify the effects of such defects on the mechanical properties of the finished composite, a study was performed on a panel in which the preform had been intentionally sheared in a controlled manner after being removed from the loom. The deviations in the preform (obtained using the protocols described in Section 3.1) are dominated by rotation of the two tow populations by about 5° relative to normal (Figs. 5.4(a–d)). Tensile test results show that the shear defects, being rather small in magnitude, have negligible effect on the *elastic* in-plane properties, consistent with predictions of classical laminate theory. For loadings *parallel* to one of the two principal tow directions, the tensile response is dictated by the tensile properties of the axial tows; the transverse tows only affect the shear and transverse normal strains. In contrast, for loadings *perpendicular* to one of the two tow populations, such

that the axial tows are slightly misaligned, the effects of misalignment are more pronounced. They give rise to accelerated strain softening, due to progressive de-coupling and unloading of the near-edge regions, and a reduced failure stress, because of the reduced fraction of axial tows that are continuous along the gauge length. The magnitude of the shear strains coupled with predictions of a laminate analysis suggest that the average matrix modulus undergoes significant reductions, by as much as an order of magnitude.
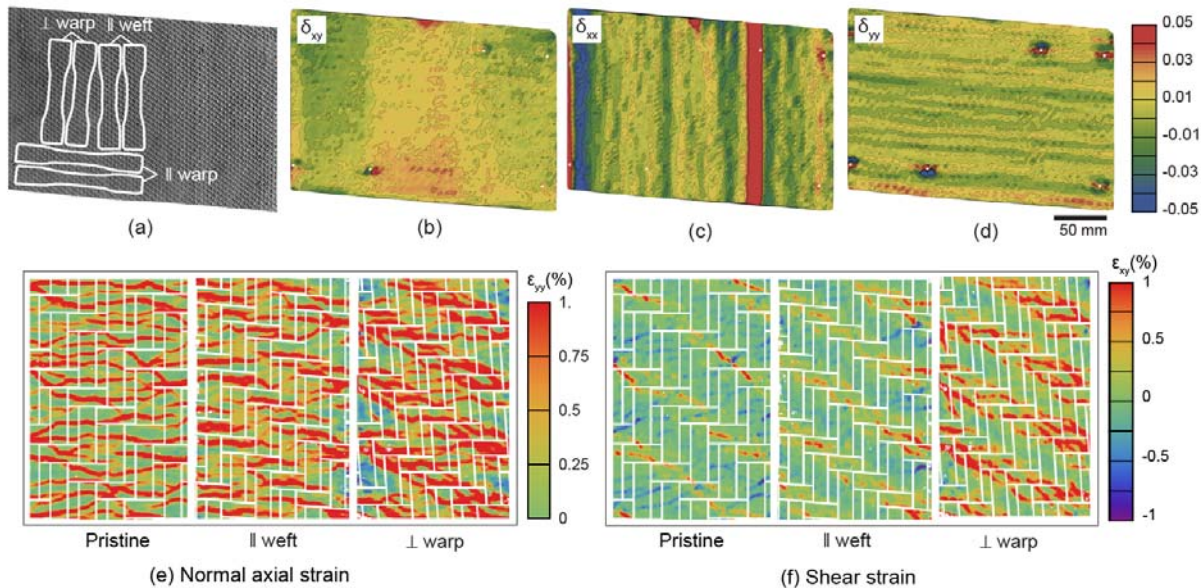

Figure 5.4: (a–d) Deviations in warp and weft tows in a sheared C/SiC preform. (e) Normal and (f) shear strain patterns upon loading pristine and sheared panels parallel to the weft direction and perpendicular to the warp direction, at a stress of 300 MPa.

5.4. Phenomenological Elastic/Plastic Constitutive Law

The nature of modeling of CMCs and the requisite degree of model fidelity for component design depend on the complexity of the microstructure (*i.e.* fiber architecture, uniformity of matrix phases, porosity, etc.), the complexity of loading (characterized by stress multi-axiality and alignment of principal stresses with fiber directions), and the length scales of interest. In simple laminates, the pertinent length scales are well defined by the fiber and ply dimensions. Here, micromechanics can be most readily applied. As the complexity of the microstructure and/or the loading increase, micromechanics-based approaches become largely intractable (except, perhaps, in providing insights into the behavior of individual tows). In this domain, more sophisticated computational models are required to predict composite behavior. At the extreme end of the spectrum – at the *macro-scale* – where the structural length scales far exceed those of the material microstructure, phenomenological constitutive models based on homogenized (but anisotropic) composite properties can be employed. These can be readily implemented in finite element simulations. Additionally, in principle, multi-scale models can be constructed by combining the latter phenomenological models with more detailed meso-scale models for the most critical regions of a structure.

The principal objective of this part of the study was to develop a phenomenological model for CMC laminates that can be calibrated using experimental data from standard mechanical tests

(e.g. tension, shear) and is applicable to common CMC fiber architectures. The study was motivated in part by the recognition that existing elastic-plastic constitutive models for CMC laminates are insufficiently general.

In its current form, the new model is applicable to two-dimensional (cross-ply-like) architectures. The predictive capability of the model has been demonstrated through comparisons of numerical simulations with full-field strain measurements in open-hole tension tests [D13]. The correlations are remarkably good (Fig. 5.5). In particular, the model accurately predicts the size and shape of the shear bands that develop at the hole edge. The magnitudes of the normal strains are also captured well, with one exception: in the experiments, strain "hot spots" emerge at the tow cross-overs (locations where undulating warp tows dive beneath flat weft tows). Such features have previously been observed in tension tests on straight (unnotched) test specimens [D3]. These relatively fine (tow-scale) variations can only be captured through computational models of the type described in Section 3. This is the subject of an ongoing study.

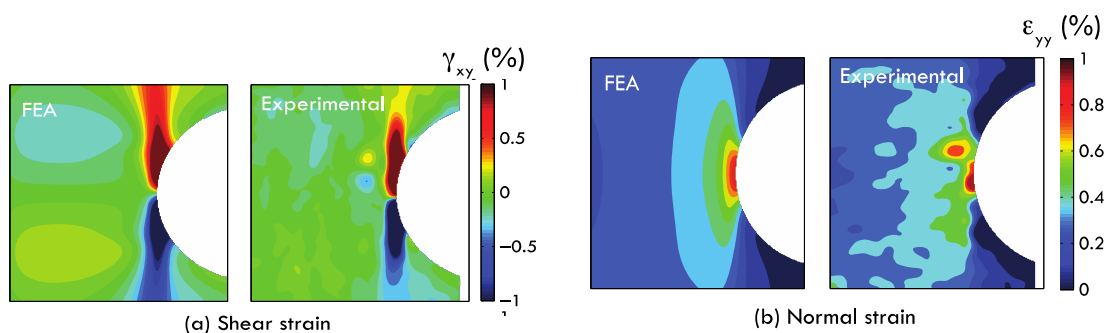(a) Shear strain   (b) Normal strain

Figure 5.5: Comparisons of computed and measured strain distributions ahead of a hole in a composite panel during tensile loading, at a stress of 350 MPa [D13].

5.4. Impact and Future Directions

The experimental and computational tools developed within the NHSC program are now impacting other (ongoing) research programs. The high-temperature imaging and strain mapping facility has generated particularly notable attention. The facility is actively being used in research programs on both environmental and thermal barrier coatings for turbine engines (PI: Carlos Levi, funded by ONR). It has also served as the focal point of a new program on the deformation and damage of 3D woven SiC/SiC composites (PI: Zok, funded by IHI Corp.). The facility was also used for high temperature testing/imaging of textile-based SiC-SiC turbine blades in an Air Force VAATE program (PIs B. Cox, D. Marshall, O. Sudre).

The *3D Geometry Generator* along with the codes for voxel-based meshing that were developed under the NHSC have been recently adapted to fiber architectures and ceramic materials of interest to gas turbine OEMs (PI: Zok, funded by Pratt & Whitney). Here they are being used in conjunction with strain mapping experiments in order to investigate the non-uniformities in strains/stresses that arise during loading (either mechanical or thermal) and to assess local damage/failure models. Such models are essential to the prediction of long-term durability of these composites in aero-engine applications. The codes are also being used in a program on particle-based computational models for damage development in CMCs (PI: Begley).

6. Numerical Methods for Discrete Damage

The goal of this study was to develop an efficient numerical analysis capability that can perform high-fidelity virtual testing of complex 3D composites under arbitrary thermal-mechanical loads. For this purpose a novel augmented finite element method (A-FEM) has been developed to perform high-fidelity analyses with explicit consideration of progressive damage evolution at various scales (i.e., fiber scale, tow/ply scale, and the macroscopic structural scale) of interest to structural engineering as well as material development. Significant breakthroughs have been made in development of numerical methods, as well as in understanding of material/structural behavior. Through a carefully designed pipeline exercise, the A-FEM method has been demonstrated to be an effective tool for virtual testing of composites.

6.1 The Augmented Finite Element Method (A-FEM)

In its original form, our A-FEM uses phantom nodes to account for the discontinuities in the thermal-mechanical fields caused by the progressive crack initiation and propagation [C1]. It enables modeling of arbitrary crack evolution in solids as long as the discrete damage processes are not directly coupled (through merging or bifurcating). By extending the augmentation method to interface cohesive zone models, we developed a suite of augmented cohesive zone elements to cope with nonlinear coupling between cracks in bulk material domains and at interface delaminations [C3].

More recently, the A-FEM was reformulated in a manner that enables it to deal with formation of multiple cohesive cracks and their interactions as they evolve [C14, C15]. This capability is the key to being able to account for arbitrary crack merging or bifurcation in heterogeneous solids such as textile CMCs. Few of the existing methods, including the eXtended Finite Element Method (X-FEM), the Phantom Node Method (PNM), the Embedded Discontinuity Method, and our previous A-FEM, can handle such difficult problems with physical consistency and numerical efficiency.

The new A-FEM does not need to use additional nodes (as in PNM) or extra nodal degrees-of-freedom (as in X-FEM) which are the major numerical burdens in handling multiple interactive cracks. Instead, we use elemental internal nodes whose degrees-of-freedom, after being used for crack displacements calculation, are condensed at elemental level. We have devised a novel algorithm that solves analytically the nonlinear equations (caused by nonlinearity in the cohesive laws) at elemental level with extreme numerical efficiency (Liu et al. 2014).[3] As a result, the elemental equilibrium (with full consideration of multiple intra-elemental cracks) is mathematically exact within the finite element context.

One of the unparalleled capabilities of the new A-FEM is that it permits repeated augmentation of an element to host multiple cracks, so that crack merging and/or bifurcation (one of the long-lasting numerical challenges for all other methods), becomes a natural outcome of the local stress environment. Hence there is no need for extensive tracking algorithms for evolving crack

---

[3] Liu, W., D. Schesser, et al. (2014). "Numerical Performance of a Consistency-Check Based Algorithm for Element Condensation in Augmented Finite Element Methods."

surfaces. Such tracking has proven to be extremely numerically burdensome, if not entirely intractable.

The new A-FEM is completely compatible with standard FEM software packages because it uses standard shape functions for stiffness integration and does not introduce any new degrees-of-freedom into a problem with evolving cracks. The element has been implemented into the commercial software ABAQUS as a user-defined element. A series of numerical performance checks have demonstrated that the new A-FEM formulation, coupled with our novel elemental condensation algorithm, enables drastic improvements in numerical accuracy, stability, and robustness. In particular, the new A-FEM enables

a) Mesh insensitive, accurate fracture predictions with mesh sizes 10 ~ 50 times larger than those reported in literature using X-FEM or PNM .

b) 2~3 orders of magnitude (100 ~ 1000 times) improvement in numerical efficiency as compared to the X-FEM in ABAQUS

c) Superior numerical stability and robustness.

The A-FEM has recently been extended to account for 3D cracking in complex textile composites [C23] and to have transient temperature degrees-of-freedom to deal with arbitrary cracking in coupled thermal-mechanical loading environment ([C21] and Do 2014[4]). Figure 6.1 gives some numerical examples that demonstrate the abovementioned performance improvements.
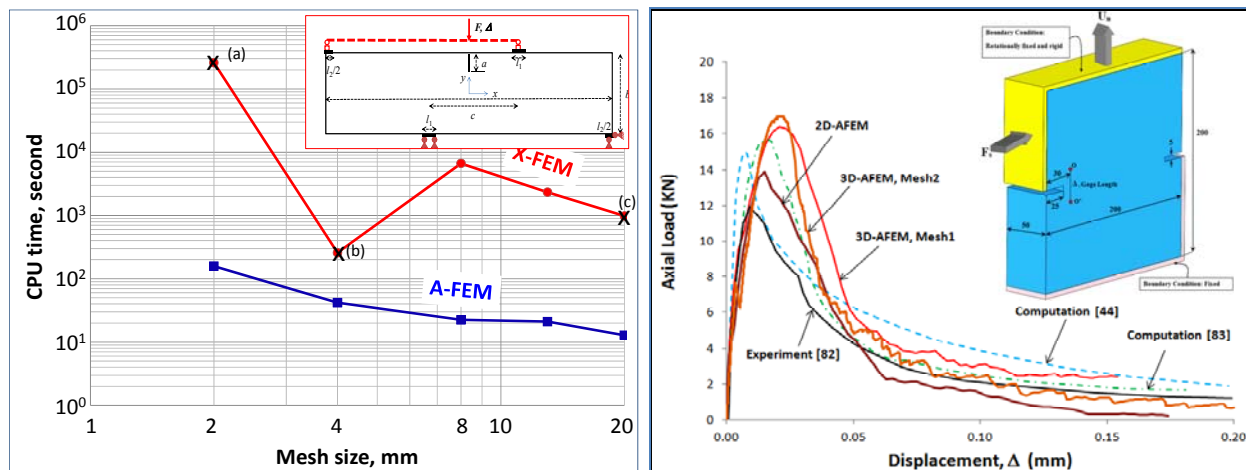

Figure 6.1 (a) Comparison of CPU times required by the 2D A-FEM and the 2D X-FEM in ABAQUS in simulating the 4-point shear beam test (inset) with 5 different meshes. The CPU time of the A-FEM is consistently 2-3 orders of magnitude less than that of the X-FEM. (b) 3D A-FEM simulated load-displacement curves of a double notched beam under combined tension and shear (inset). The A-FEM element number is 4 times less than that used in literature yet the simulated results are more accurate as compared to the experimental results.

---

[4] Do, B. C. (2014). Extending the Novel A-FEM to Model Arbitrary Cracking in Thermo-Elastic Solids. PhD, University of Miami.

6.2. A-FEM for Understanding Multiscale Materials/Mechanics Issues

The newly developed A-FEM modeling capabilities have enabled simulation of the mechanical behavior of complex heterogeneous materials with unprecedented fidelity. The most important enabling achievement of the A-FEM is that it allow for accurate accounting of the microscopic material damage evolution processes and for quantifying their explicit influence on macroscopic structural integrity. A recent success in high-fidelity modeling of a laminated composite is given in Figure 6.2.
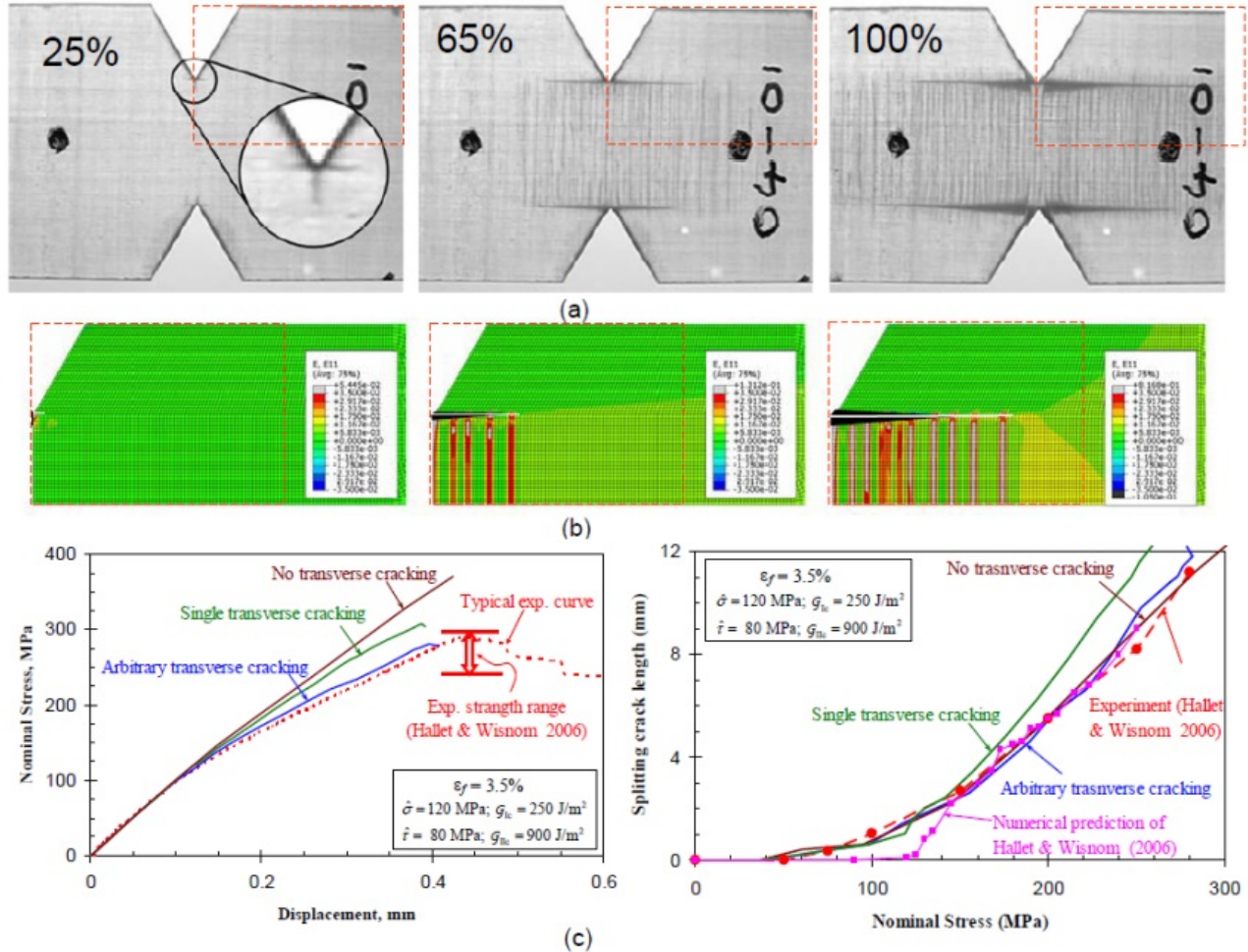

Figure 6.2 (a) Experimentally observed damage processes in a DNT specimen; (b) predicted damage evolution using our A-FEM; and (c) direct comparison of stress-displacement curves (left plot) and splitting crack growth as a function of applied stress (right plot).

Figure 6.2 compares experiments for a double-notched tension (DNT) specimen with simulations using embedded CZMs calibrated by independent literature data. All crack initiation and propagation (multiple transverse ply cracking, longitudinal splitting, interlaminar delamination, and distributed nonlinear shear damage) were determined automatically in the simulation by interrogating the current stress state. The predicted damage evolution correctly captures the complete crack scheme seen in experiments, including all crack locations, sizes, and shapes

(Fig. 6.2a vs. Fig. 6.2b). The predicted load vs. displacement curves and splitting crack length vs. applied stress are in excellent quantitative agreement with experiment (Fig. 6.2c) and the scatter in predicted strength due to scatter in measured material fracture properties matches the scatter measured in tests [C3].

The fact that this high-fidelity analysis was achieved within a single structural model so that all processes occur concurrently, as opposed to the common strategy of hierarchical homogenization, is unprecedented.

An important conclusion from this example is that, to achieve high fidelity in progressive composite damage analyses, all major damage processes and their interdependence must be explicitly modeled by embedding failure/damage descriptions in the form of nonlinear cohesive zone models in the structural model. Further, such nonlinear descriptions can be obtained through A-FEM models at relevant, smaller scales [C1]. This presents a big step towards virtual testing of composite materials.

6.3 A-FEM for Virtual Testing of CMCs: The Pipeline Exercise

The improved understanding of microscopic progressive damage evolution in macroscopic structural integrity enabled by the A-FEM-based virtual testing capability has been recently demonstrated through a concerted comprehensive exercise involving several research groups within the NHSC. In this exercise, detailed microstructural information from an actual 3D textile CMC specimen (C/SiC, Fig. 2.2.), including the fiber tow geometry and spatial distribution was carefully characterized by x-ray microscopic computer tomography (μCT) (at UC-Berkeley). The information was then subjected to an extensive statistical analysis and the result was employed by a virtual specimen generator to generate virtual specimens with realistic statistics (at UCSB and Teledyne). The virtual specimen was then converted into finite element mesh and subjected to the 3D A-FEM analyses. The progressive damage of the virtual specimen predicted by A-FEM was then compared to the physical testing results conducted in UCSB.

In the 3D A-FEM analyses, all the material properties and damage descriptions were either calibrated from literature data or from fiber-scale representative volume element analyses using the A-FEM and the augmented cohesive zone elements [C3, C18]. The comparison of the A-FEM-predicted and experimentally measured cracking of the specimen is given in Figure 6.3. The Textile preform coated with a thin layer of matrix is shown in the left micrograph in Figure 6.3(a). A specimen with a fully infiltrated matrix that was analyzed by μCT is shown in Figure 6.3(c). Note that the μCT characterization indicated that matrix cracks that had formed above a weft tow segment arrest when they approach the region where a warp tow crosses over the weft tow. The A-FEM predicted crack pattern is shown by the right micrograph of Figure 3(a). Compared to experimental observations of microcracks by digital image correlation shown in the center micrograph of Figure 6.3(a), all key features of the crack pattern—including the approximate periodicity of the microcracks, which form above near-surface weft tows, and the alignment of microcracks in diagonal bands (one of which is outlined by the ellipse)—are well replicated by the A-FEM analysis. Figure 6.3(*b*) shows a detailed rendering of a simulated microcrack above a weft tow that is correctly predicted to arrest upon approaching the underlying warp tow. The matrix containing the crack is present in this image, but the matrix elsewhere was stripped away in rendering the image to reveal the underlying tow architecture.

With the help of such analyses, it is now understood that the surface crack propagation along the weft direction is deterred in the warp tow crown region due to the local straightening of the warp tow, which reduces the surface tensile stress necessary to drive the crack to propagate along this direction. In such locations, the crack may instead propagate into the specimen and circumvent the warp tow from its bottom, or, induce delamination between the warp tow and the surrounding matrix (not seen from Figure 6.3b).

This level of understanding of microcrack propagation would not be possible without the detailed A-FEM analyses. Further understanding of important issues such as what are the dominant parameters that control matrix cracking or tow/matrix delamination, and what are the possible means to mitigate such cracking events, is currently under investigation.
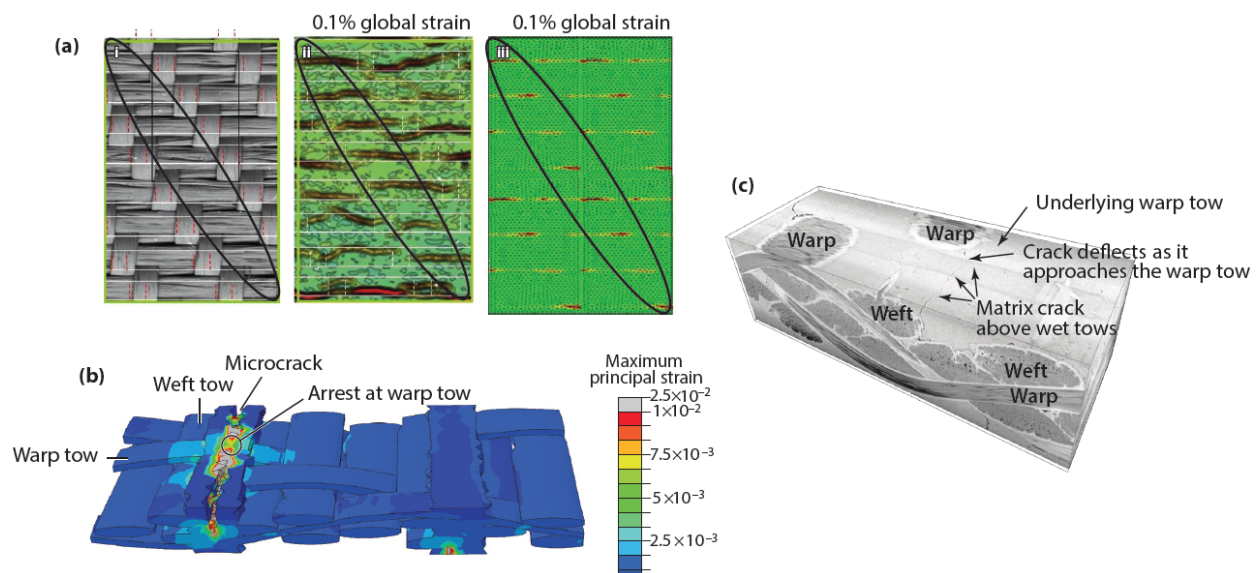

Figure 6.3   (a) Comparison of A-FEM predicted (right micrograph) and experimentally measured (center micrograph) band-like distributed surface cracking under in-plane tension. (b) Zoom in of an A-FEM predicted surface crack showing the crack propagation deterred at the crown region of a warp tow, which is responsible for the band-wise crack distribution observed experimentally. (c) 3D visualization of the specimen from the μCT data.

6.4. Impact and Future Directions

Several activities are under way to transfer the unique capabilities of augmented finite element method (A-FEM) to the Army Research Laboratory and other DOD researchers. These include use of the code in internal ARL programs; funding of a grant to Prof. Yang for further development of the method, including to account for high strain-rate effects in polymer-matrix composites; and working with AFRL to transfer of the compiled code into a simulation platform for use by all DoD Researchers. The A-FEM method is regarded as one of the leading candidates for overcoming current gaps in computational capabilities for accurately representing complex failure mechanisms in microstructurally heterogeneous materials.

The A-FEM /Virtual Test plays a central role in a current AFRL program on life modeling for SiC-SiC composites led by Teledyne (Brian Cox) with partners Honeywell, UES, University of Miami, and UC Berkeley. The program aims to extend the work done in this NHSC program to

incorporate physical models of the interaction of microcracking and environmental degradation at high temperature into the A-FEM via the constitutive laws for cohesive zones. It combines the geometry generation capability (Section 3) and high temperature μ-CT measurements.

The A-FEM will also be used for damage simulations in new ONR program led by Teledyne (David Marshall) with partners UTRC and University of Miami to develop technology for CMCs with 3-D reinforcement architectures optimized for turbine blades and vanes.

7. Atomistic Structure Modeling and Property Simulations

7.1 Structure Modeling and Property Simulations

DFT-simulations of amorphous SiCO structures

Extensive modeling of amorphous silicon oxycarbide ceramics, ranging from glassy SiCO to SiCO containing "free" carbon was performed at UTA. Particular emphasis was placed on possible interface structures that may connect the "free" carbon phase to the SiCO glass. Model structures were generated using an in-house network modeling algorithm which allows incorporation of different hypotheses of atomic arrangements into the model (Fig. 7.1). The models are subsequently treated within density functional theory including *ab initio* molecular dynamic simulations. This set of disordered network-based models was augmented by "melt-quench" models generated using *ab initio* molecular dynamic simulations via quenching melt-like SiCO(:H) structures.

Upon analyzing structure and energy of optimized models, the enthalpy of formation of glassy SiCO was found to increase with increasing phase content of SiC. Models with high SiC content show a pronounced tendency of forming SiC-rich clusters embedded in glass. No support was found for a favorably bonded interface between glass and "free" carbon, neither via a SiC-rich interface nor via direct bonds between Si and sp^2-C. Instead, the two phases may coexist separated even with the expense of dangling bonds at the edge of the carbon phase. Our modeling indicates that such a separation is driven by the low surface tension of silica glass.
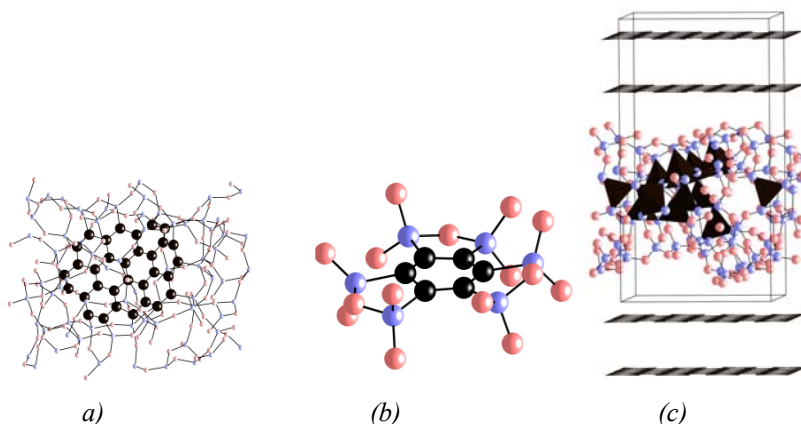

| *a)* | *(b)* | *(c)* |

Fig. 7.1. Network models constructed and optimized using DFT calculations. (a, b) Models showing "free" C embedded in a glass matrix via direct bonds between Si and sp^2-C. (c) A SiCO glass slab-model with grapheme sheets dispersed between the slabs. Note that the slab surface is composed by Si-O bonds, while the SiC-rich part (represented by dark CSi4-tetrahedra) is embedded in the glass.

Hypothetical Crystalline SiCO –– Analyzing the Materials Genome

More than 10,000 ordered crystalline structures of SiCO were generated and studied with help of the AIRSS (Ab Initio Random Structure Simulations) algorithm and the USPEX-code (Universal Structure Predictor: Evolutionary Xtallography). Under the assumption that for a given composition a well-ordered crystalline structure will have a lower enthalpy of formation (from elements or constituent phases) than an amorphous structure, we searched for low-energy

crystalline models of SiCO that may help rationalize the proposed thermochemical stability of some SiCO ceramics. Moreover, such crystalline structures may serve as approximants for structure and energy of glassy phase of the same composition.

The results support the key ideas about the most favorable local structures in SiCO: the presence of silicon mixed tetrahedra and CSi_4 units that represent the main features of stoichiometric SiCO ceramics. However, we did not find indication for stability of ternary SiCO with respect to its binary compounds, q-SiO_2 and β-SiC. All well-ordered structure models exhibit positive enthalpy of formation. A "free" carbon phase bonded to the SiCO destabilizes crystalline structures even more and no favorable interface formation was observed. Through careful analysis of energetics, we can attribute the reason for this increase in instability to the formation of a C-**C-Si**-O bonding interface, hence, to direct bonds between Si and sp^2-C.

Therefore, amorphous models and crystalline approximants alike indicate that a covalently bonded interface between SiCO glass matrix and the embedded "free" carbon is energetically unfavorable.

Molecular Dynamic Simulations of amorphous SiCO using classical potentials

The structure of SiCO ceramics with "free" carbon was modeled using a Tersoff-style empirical potential. The goal was to rationalize the dispersion of the free carbon within the "domain model" proposed by Saha and Raj.[5] The models comprise 1,000,000 to 1,500,000 atoms and are generated using a standard melt-quench approach. With a fixed ratio SiC:SiO2 = 1:4 (20 mol% SiC in the glass phase), systems with C_{free}/Si ratio of 0, 1:1 and 2:1, (from glassy SiCO to C-rich SiCO) were investigated (Fig. 7.2).
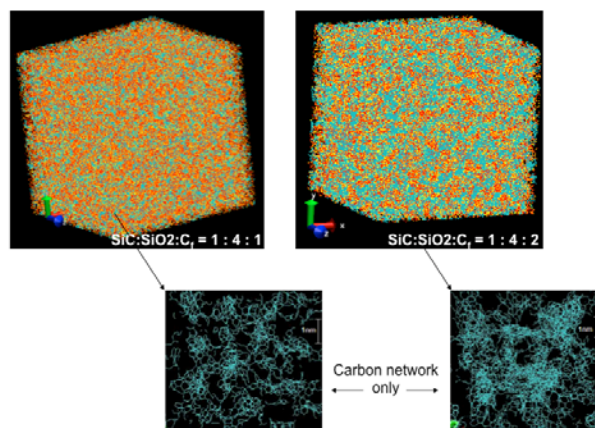

Fig. 7.2. Million-atom structures (top) and carbon substructures (blue filament) of SiCO ceramics with different ratio C/Si. Full size of the periodic models is ≈ 7 nm.

A strong correlation was found between carbon content and dimensions of carbon as well as glass domains in the structure: the higher the carbon content, the larger the extent of carbon segregations (in both lateral size and thickness) and the smaller the size of glass domains. This corresponds nicely to experimental observations of Saha and Raj. However, the empirical potential simulations do not indicate a SiC-rich interface between glass carbon segregations as has been hypothesized.

---

[5] Saha, A., Raj, R., & Williamson, D. L. (2006). A Model for the Nanodomains in Polymer‐Derived SiCO. *Journal of the American Ceramic Society*, *89*(7), 2188-2195.

Simulations of mechanical properties of SiCO ceramics at room temperature yield results for Young's modulus and maximum yield strength comparable to experiment (Fig. 7.3). Simulations at elevated temperatures show a decrease of the Young's modulus with increasing temperature.
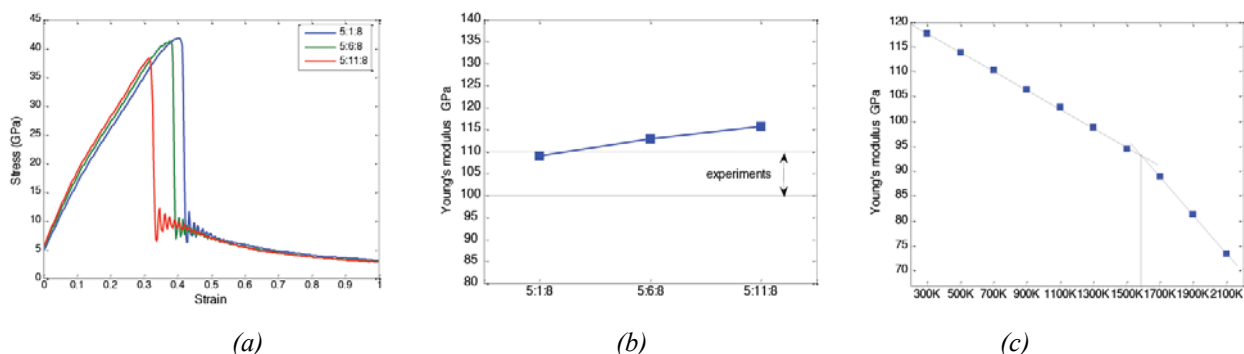

(a)	(b)	(c)

Fig. 7.3. Mechanical properties of SiCO obtained by million atoms simulations using a Tersoff potential. (a) Tensile stress-strain response as a function of composition. (b) Young's moduli of SiCO for different compositions and comparison with experiment. (c) Young's modulus of C-rich SiCO as a function of temperature.

Structure and thermochemistry of metal oxide silica glasses

Driven by experimental efforts on oxidation of UHTC and glass synthesis by the MS&T group, models were developed for glass structures of metal oxides (MOx) dissolved in boria (B_2O_3) or silica (SiO_2), for M = Hf, Nb, Ta, Mo, and W (Fig. 7.4). Use of the melt-quench approach together with *ab initio* molecular dynamic simulations provided a realm of structures with different amount of metal oxides.The models yielded significant structural trends, together with computed thermochemical data.

In the simulations, the coordination numbers (CNs) of metal cations dissolved in the glass turn out to be a function of the mole fraction of the metal oxide: the higher the mole fraction, the higher the average CN. Higher mole fractions always go along with the trend to form agglomerates. Such metal oxide agglomerates may cause a lower diffusivity of oxygen in such glasses and may be responsible for the observed higher oxidation resistance.
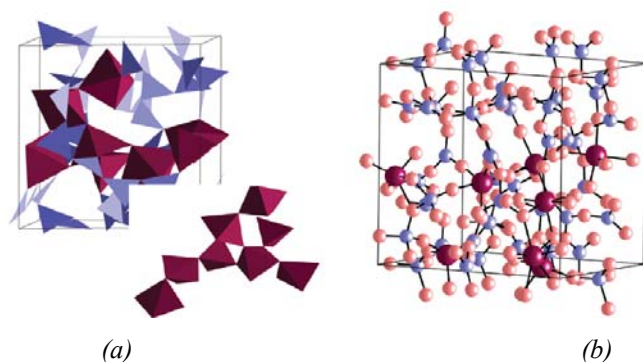

(a)	(b)

Fig. 7.4. (a) Model of Nb_2O_5- B_2O_3 with molar ratio 4:18. The inset shows the fused NbO_x-polyhedra of the structure. All eight Nb atoms agglomerate to form a NbO_x-cluster. (b) Model of WO_3-SiO_2 with WO_x-segregation.

The thermochemical data of MO_x-B_2O_3 and MO_x-SiO_2 systems is summarized by the enthalpy of mixing, ΔH_{mix} (Fig. 7.5). The quantity varies very strongly, albeit the data shows a trend favoring the mixing of "smaller" cations such as molybdenum. Moreover, there are differences in solubility of metal oxides in boria or silica, even given an error margin of 0.2 eV per cation in the data.

	SiO_2	B_2O_3	
HfO_2	+0.8	+0.5	S higher in B_2O_3
Nb_2O_5	+0.7	+0.6	
Ta_2O_5	+0.4	+0.5	
MoO_3	+0.1	+0.3	S higher in SiO_2
WO_3	+1.0	+1.1	

Fig. 7.5. Summary of the enthalpy of mixing, ΔH_{mix} (in eV/metal cation), of metal oxides in boria and silica for low metal oxide content (dilute limit). The error margin is about 0.2 eV/metal cation.

The phase diagram B_2O_3-SiO_2: indication for a region of stability

Modeling mixtures of boria and silica within the quasi-binary system B_2O_3-SiO_2 shows nice agreement of the computed enthalpy of formation ΔH_f with experimental data. Thus, it came as a surprise when we found a region of stability for a composition of 33 mol-% B_2O_3 (Fig. 7.6). Glass structures generated with this composition have a lower enthalpy of formation than a combination of glass structures of SiO_2 and B_2O_3. The trend, albeit quite small (0.04 eV/cation, equal to about 4 kJ/mol), has been confirmed through modeling of several independent structures. A search of crystalline structures with composition $B_2Si_2O_7$ revealed two models, for which the energy towards decomposition into the lowest energy crystalline polymorphs of is SiO_2 and B_2O_3 essentially zero. Hence, it may be possible to synthesize a glass with composition $B_2Si_2O_7$ and, subsequently crystallize it to adopt this new structure.
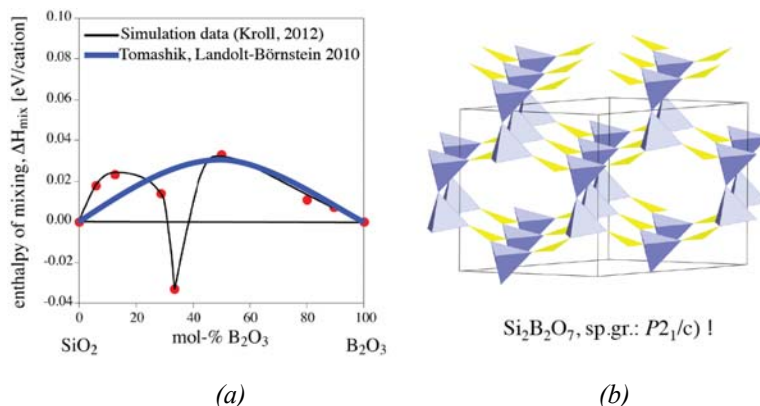

(a)   (b)

Fig. 7.6. (a) Computed enthalpy of mixing, ΔH_{mix} (in eV/cation), in the B_2O_3-SiO_2 glass system (with reference to amorphous B_2O_3 and SiO_2) and comparison with compiled experimental data. (b) Proposed crystal structure of $B_2Si_2O_7$ with vanishing enthalpy of formation with respect to the crystal structures of α-B_2O_3 and α-quartz-SiO_2.

7.2 Mechanistic Studies

Diffusion of O_2 and CO in Vitreous Silica and SiCO glass

Density functional theory calculations were combined with the climbing image nudge elastic band (CINEB) method to calculate diffusion barriers of O_2 and CO in silica glass and SiCO glass (Fig. 7.7). Assessment of several diffusion paths in both amorphous systems indicates that energy barriers to diffusion are higher for both species in SiCO than in SiO_2. Thus, the diffusivity of both species is expected to be smaller in SiCO. Comparing the two molecules with each other, we find that within the same host matrix CO will diffuse less easily than O_2. We conclude that oxidation of SiCO and formation of a clean interface towards SiO_2 is governed by formation and diffusion of CO in the glass, since only outgassing of CO allows for new O_2 to enter the system.
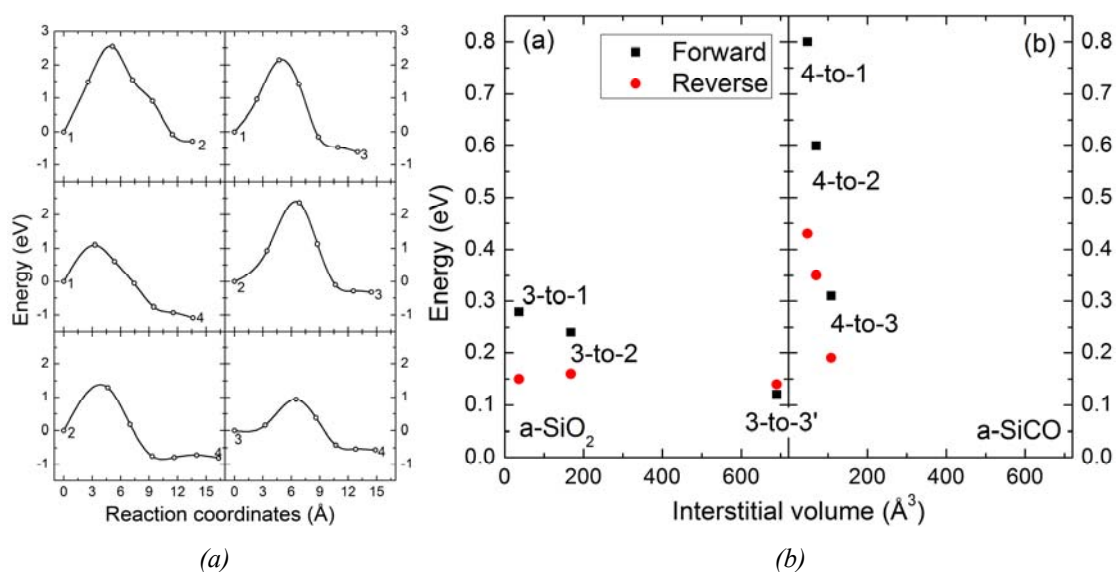

(a)	(b)

Fig. 7.7. (a) Typical energy profile for diffusion of O_2 in amorphous SiCO. The barrier for the diffusion path is computed as the difference between initial point of the migration and maximum energy along the path. (b) Computed diffusion barrier differences between O_2 and CO in amorphous silica and SiCO. Positive values indicate that the barrier for CO migration is larger than that for O_2 migration. The integer numbers are labels for open space (voids) inside the structure models.

Oxidation mechanisms in glassy SiCO ceramics

Minimum energy paths of O_2 molecules reacting within a model of SiCO glass were computed. While diffusion processes have been accessed separately, the focus here is on reactions with the network (i.e., forming new bonds). A single O_2 inserted into the structure attacks C sites in SiCO. However, formation of a CO molecule by reacting a single O_2 with sp^3-C inevitably creates Si-Si bonds. The calculated energy of formation is more than 5 eV.

A path with significantly lower activation energies, corresponding to faster kinetics, was found when inserting two O_2 molecules into the SiCO glass structure. The calculated full kinetic path is shown in Fig. 7.8. Essentially, a first O_2 "activates" a C site forming a Si-O-O-Si (peroxyl) and a Si-O-C linkage. A second O_2 reacts with the same C site and facilitates ejection of a CO molecule. Crucial energy barriers are those for a second O_2 (about 2 eV) and ejection of the CO

from the network (about 1.5 eV), both significantly lower than 5 eV for reacting a single O_2. Thus, we conclude that oxidation of SiCO glass and formation of CO necessitates an "activation" step first, with a second oxygen molecule required to release CO.
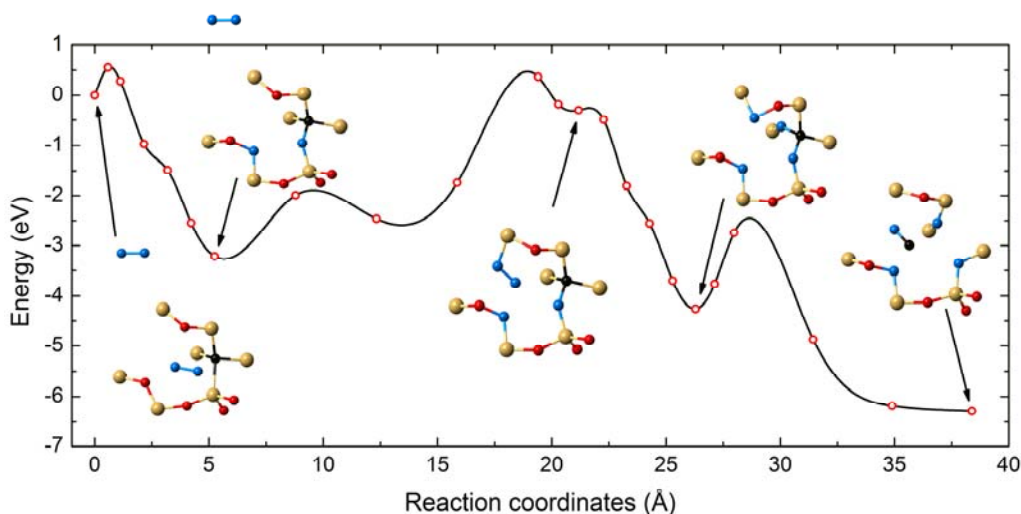

Fig. 7.8. *Computed kinetic path of oxidation in SiCO. Oxygen atoms of O2 molecules are blue spheres, while network oxygen atoms are red spheres. Yellow spheres are Si atoms. Black spheres are C atoms. The first O_2 molecule "activates" the network. Formation of interstitial CO happens only once a second O_2 molecule reacts with the network.*

7.3 Method Development

Computing thermal conductivity of solids at elevated temperatures by ab-initio MDsimulation

A method was developed to extract data for the lattice thermal conductivity k of disordered structures from *ab initio* molecular dynamic simulations. The approach applies kinetic theory to relate thermal conductivity k to the lifetime τ, mode heat capacity c_V, and group velocity v of the phonons. The essential part of the method is to evaluate the lifetime τ by fitting the spectral density of the system to a series of Lorentzians, each Lorentzian corresponding to a phonon with life-time related to its width. While the application is not simple (it requires manual fitting and filtering of noisy signals) we were able to compute thermal conductivities of several crystalline materials, such as β-SiC, and many amorphous structures and glasses (a-SiC, a-SiO$_2$). Comparison with experimental data – where available – showed very good agreement (Fig. 7.9).
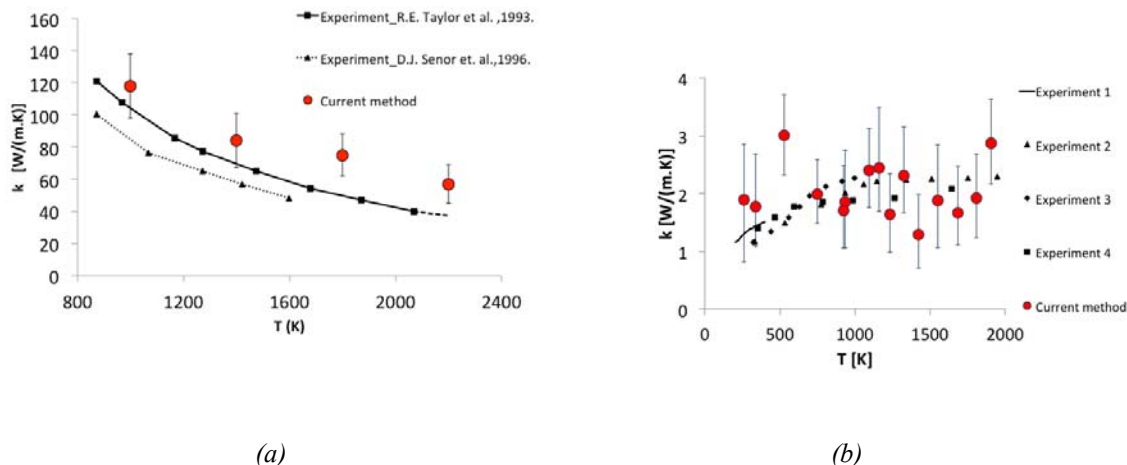
(a)

(b)

Fig. 7.9. Thermal conductivity computed for crystalline β-SiC (left) and amorphous a-SiO₂ (right) together with experimental data.

Supporting structure analysis of SiCO ceramics by 29Si NMR spectroscopy –– ab initio computation of chemical shifts

Harvesting data computed for hundreds of structural models of SiCO, we quantified relations between chemical shifts and structural properties, namely Si-O-Si bond angles, for different chemical environments of Si in SiCO (Fig. 7.10). Using these relations, an experimental ^{29}Si NMR spectrum can be transformed into angle distributions for Si-O-Si angles at a Si site. Each distribution obtained for the various mixed tetrahedral, SiC_nO_{4-n}, is independent and allows extraction of extended information. While the hybridization of the C (sp^2 or sp^3) coordinating to Si significantly impacts the chemical shift (with differences of about 7 ppm), the Si-C bond length plays no significant part in the structures tht were modeled.

The present method produces results consistent with experimental diffraction data. The results show that it is possible to determine the interface connectivity based on the shape of the experimental $SiCO_3$-peak, when the SiO_4-peak is used as a baseline. All experimental data we surveyed agrees with the notion that in ceramics annealed at 1000°C bonds exist between Si and sp^3-C. No evidence was found for bonds between Si and sp^2-C: an upper limit of 5% (of all Si-C bonds) was estimated, based on the signal-to-noise ration of experimental data.

Moreover, we find a significant portion of large-angle Si-O-Si entities in all C-rich SiCO ceramics. Since these entities resemble structure elements seen in zeolites, we hypothesize that C-rich SiCO comprises (large) cages and voids into which the free carbon phase is segregated. Overall, analysis of experimental 29Si NMR data presents a picture in good agreement with the structural modeling pursued for SiCO ceramics.
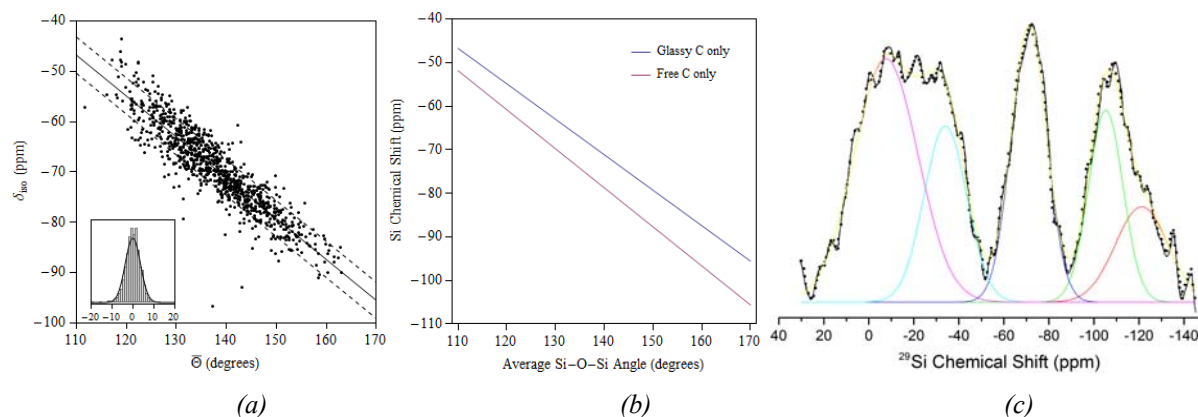
Fig. 7.10. (a) 933 Si centers contributing to the linear correlation between the three adjacent Si-O-Si angles and the chemical shift observed at the Si site. (b) Angular correlation functions for conductivity computed for $SiCO_3$-environments. The two different curves reflect bonding of Si to sp^3-C (glassy) and sp^2-C. (c) Experimental 29Si NMR spectrum for a C-rich SiCO. The SiO_4-peak shows substantial contribution from a 2nd component centered at ~ -120 ppm corresponding to large angles in the structure. The majority component of the SiO_4-peak is consistent with the angle distribution derived from the $SiCO_3$-peak (assuming bonding to sp^2-C). Absence of a 2nd component in the $SiCO_3$-peak reveals that no significant amounts of direct bonds between Si and sp^2-C exist.

7.4 Impact and Future Directions

Two new programs have begun that make use of and extend atomistic modeling carried out in the NHSC program. One is a DARPA program in which UTA (P. Kroll) is teamed with Teledyne (O. Sudre) to find new chemical routes for producing the high pressure cubic phase of boron nitride. This involves manipulation of precursor polymers to promote early formation of tetrahedrally bonded B, with parallels to the tetrahedral bonding predicted in the NHSC program near W dopants in boron-oxide glasses. The other is an NSF-grant through the Materials Genome Initiative "Multiscale Design of Hard and High Temperature Resistant Coatings by Computation and Experiment" awarded to a team from UTA (Kroll, Jiang and Meletis) and University of Minnesota (Dumitrica). The materials systems are SiBCN and ZrBCN (both with small amounts of C) synthesized with sputtering techniques. This program will draw upon several results from the NHSC program: structure and energy of boro-silicate glasses, nano-scale segregations that change structure and properties; transport of species (oxygen) through a melt or glass.

8. High Temperature Materials in the System Hf-Si-C-N-O

The processing, phase evolution and oxidation resistance of ceramics made from Hf, Si, C, N, and O were investigated. Notably this system merges non-oxide ceramics with oxide ceramics at the molecular level by processing from liquid polymers that contain the desired chemistry. Additionally, nanoparticles of hafnia were incorporated into the polymers for the purposes of increasing the content of the oxide phase and enabling infiltration of fiber preforms with a ceramic matrix constituted from HfSiCNO.

The HfSiCNO materials apparently evolve into self-healing surface layers under oxidation that are constituted from $HfSiO_4$, HfO_2 and SiO_2. With further research, there is the potential of creating graded microstructures that are tailored, through materials selection and processing, to perform at temperatures up to 1600 ^{o}C in extreme environments. The coefficient of thermal expansion of $HfSiO_4$ needs to be determined but, from phenomenological experiments, it appears to be compatible with SiC. The intrinsic oxide–non oxide nature of these materials implies that they can potentially combine the mechanical resistance of carbides, with the oxidation resistance of oxides.

An additive manufacturing system was invented for infiltrating fiber preforms with polymer-derived HfSiCNO material and thereby create a high-temperature ceramic matrix. Preliminary results show high promise for this technology.

In a parallel effort, nanocomposites of HfO_2 and SiC of varying compositions were investigated, with promising results for oxidation resistance, mechanical strength, and thermal conductivity. These nanocomposites hold promise as new ultrahigh temperature ceramics for structural applications

Three key results are presented in the following summary: (i) The influence of Hf/Si ratio on the oxidation behavior of HfSiCNO ceramics, (ii) oxidation behavior of SiC fiber preforms that are infiltrated with hafnia nanoparticles-slurries, and (iii) the oxidation, and mechanical properties as well as the thermal diffusivity of HfO_2–SiC nanocomposites. The oxidation experiments are carried out at 1500 – 1600 ^{o}C (~2700 – 2900 ^{o}F) in ambient air, and in streaming water vapor.

8.1 Oxidation Behavior of HfSiCNO Ceramics Prepared from the Polymer Route

The nanodomain structure of SiCNO polymer derived ceramics is based upon the strong bonds formed by Si with C as well as with O.[6] In this sense, Hf is equivalent to Si, and it has been appropriate to specify the composition of HfSiCNO materials by the Hf/Si ratio. Ceramics with Hf/Si ratios up to 0.22 remain as solid solutions in the amorphous solid in the as prepared state [B8, B14]. At higher concentrations, HfO_2 precipitates during pyrolysis of the polymer. The study of oxidation of HfSiCNO prepared in this way provides insights into the development of a top layer of $HfSiO_4$ which appears to be self-healing in high temperature water vapor environments.

---

[6] Saha, A., Raj, R., & Williamson, D. L. (2006). A Model for the Nanodomains in Polymer‐Derived SiCO. *Journal of the American Ceramic Society*, *89*(7), 2188-2195.

The oxidation of HfSiCNO in water vapor environment differs significantly from oxidation in ambient air. In ambient air HfSiO$_4$ forms precipitates within the silica passivation layer, and the sample continues to gain weight [B9]. However, in streaming water vapor environment silica is lost, thus leading to recession and weight loss. In this instance, as silica is lost, the precipitates of HfSiO$_4$ apparently coalesce to form a continuous top coat which protects against further weight loss.

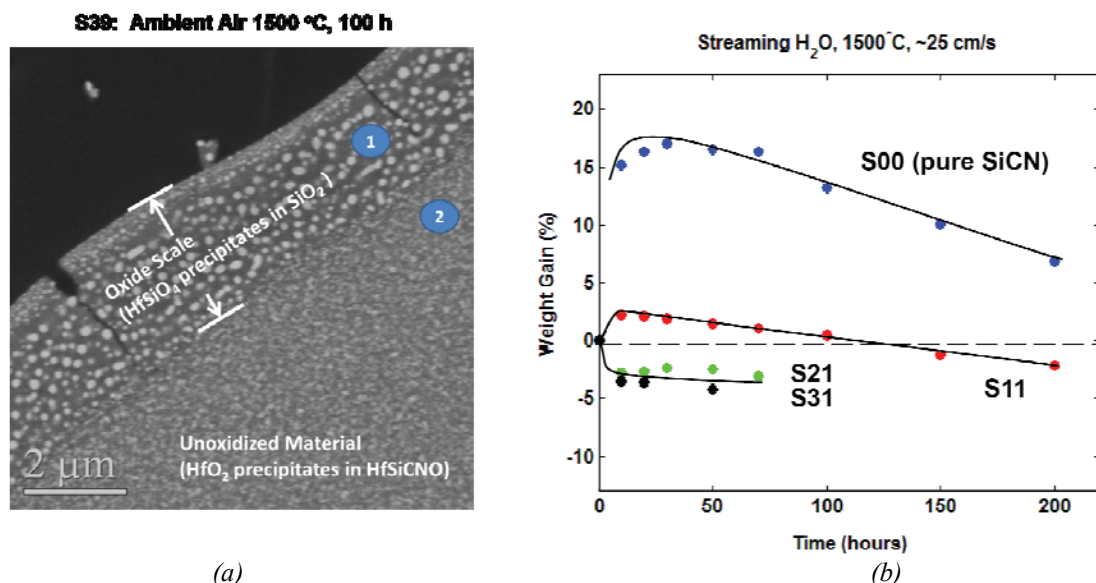(a)   (b)

Figure 8.1. (a) Precipitation of hafnon within silica oxidation scale formed in ambient air. (b) Weight changes during oxidation experiments in streaming water vapor (25 cm/s). Weight loss is suppressed in high Hf/Si compositions as the evaporation of silica leaves behind hafnon, which protects against further weight loss. The values of xx in the Sxx designation indicate the Hf/Si ratio in HfSiCNO, e.g., S31 represents Hf/Si = 0.31

The micrograph in Fig. 8.1a shows the oxidation overgrowth in dry air, which contains both silica and precipitates of HfSiO$_4$, formed by the reaction between silica and HfO$_2$. Figure 8.1b shows the change in weight when oxidized in streaming water vapor. For materials with low Hf/Si concentration (up to 0.11) the weight loss continued for at least 200 h, since a continuous layer of HfSiO$_4$ was not able to be established. However, in materials with higher Hf/Si ratios (0.21 and 0.31) the weight loss stabilized, presumably by the growth of a continuous layer of HfSiO$_4$ on the surface. The HfSiO$_4$ appears to remain stable in water vapor environment, thus producing a self-healing effect.

8.2 SiC Fiber Preforms that are Infiltrated with Hafnia Nanoparticles-Slurries

Fiber preforms can be infiltrated with slurries of HfO$_2$ nanoparticles dispersed in the liquid polymer precursor for SiCN(O). In this way it seems feasible to obtain dense matrix of the polymer derived ceramic. The cross section of the CMC fabricated in this way (after pyrolysis of the polymer) is shown in Fig 8.2. These initial results hold promise for producing dense ceramic matrices.
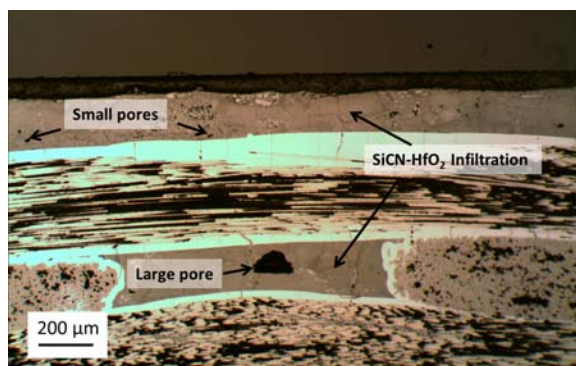
Figure 8.2: Cross section of fiber preform infiltrated and pryrolyzed with HfO2/SiCN in 2:1 ratio by weight (optical micrograph).

The composite shown in Fig. 8.2 was exposed to streaming water vapor (29 cm s^{-1}) at 1500 °C for 275 hours. SEM micrographs of the graded compositions developed during this procedure are shown in Fig. 8.3. Continuous coating of HfSiO$_4$ forms on the surface of the composite. Below that we note that SiO$_2$ has formed from oxidation of SiCN, which had partially reacted with HfO$_2$ to produce HfSiO$_4$. At greater depths unoxidized phases of SiCN and HfO$_2$ are observed.

At outer surface   **At 100 µm depth**   **At 300 µm depth**

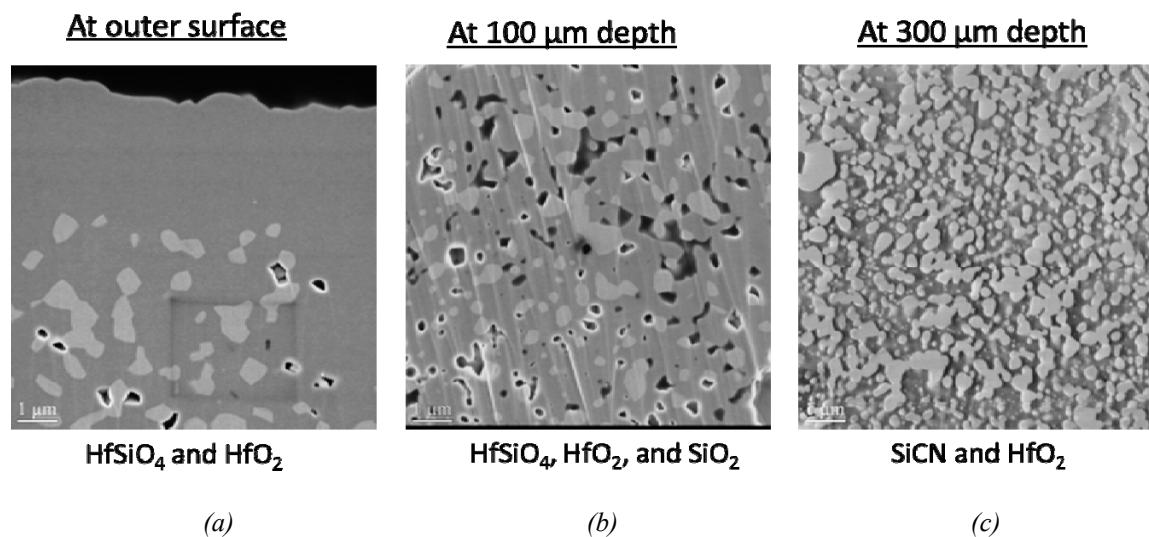HfSiO$_4$ and HfO$_2$ HfSiO$_4$, HfO$_2$, and SiO$_2$ SiCN and HfO$_2$

(a)   *(b)*   *(c)*

Fig. 8.3. SEM images of graded compositions developed during exposure to streaming water vapor (29 cm s^{-1}) at 1500 °C

8.3 HfO$_2$–SiC Nanocomposites

Since polymer derived SiCNO and SiC oxidize with similar kinetics to produce silica, attempts were made to study the oxidation and self-healing behavior of HfO$_2$-SiCN composites with the model system constituted of polycrystalline HfO$_2$-SiC. These nanocomposites were prepared by SPS. They were oxidized at 1600 °C in air for 10 hours. The thickness of the oxidation scale was measured and its effect on mechanical properties was measured. The thermal conductivity of the composites, which can be of interest in ultrahigh temperature applications, was measured. The SiC content in the nanocomposites was varied from 10 vol% to 90 vol%. A common feature of

these composites is that grain growth is suppressed during hot consolidation yielding grain size of the order of 200 nm. The fine grain size imparts high fracture strength to these composites [B15].

The results from these experiments (a collaboration with Dr. Shinoda at Tokyo Institute of Technology) are given in Fig. 8.4. The highly non-linear influence of the SiC content on the growth of the oxidation scale and on the thermal diffusivity is quite remarkable. The high thermal diffusivity, and very low grain growth during processing, imply strong interfacial bonding between SiO_2 and SiC [5]. The sharp drop in the rate of oxidation is attributed to the silica-rich structure that would develop upon oxidation, as illustrated by the composition diagram on the bottom right. While much further evaluation of these results is warranted, they offer the specter of a new class of ultrahigh temperature ceramics which have high strength [B15], good oxidation resistance and high thermal conductivity.

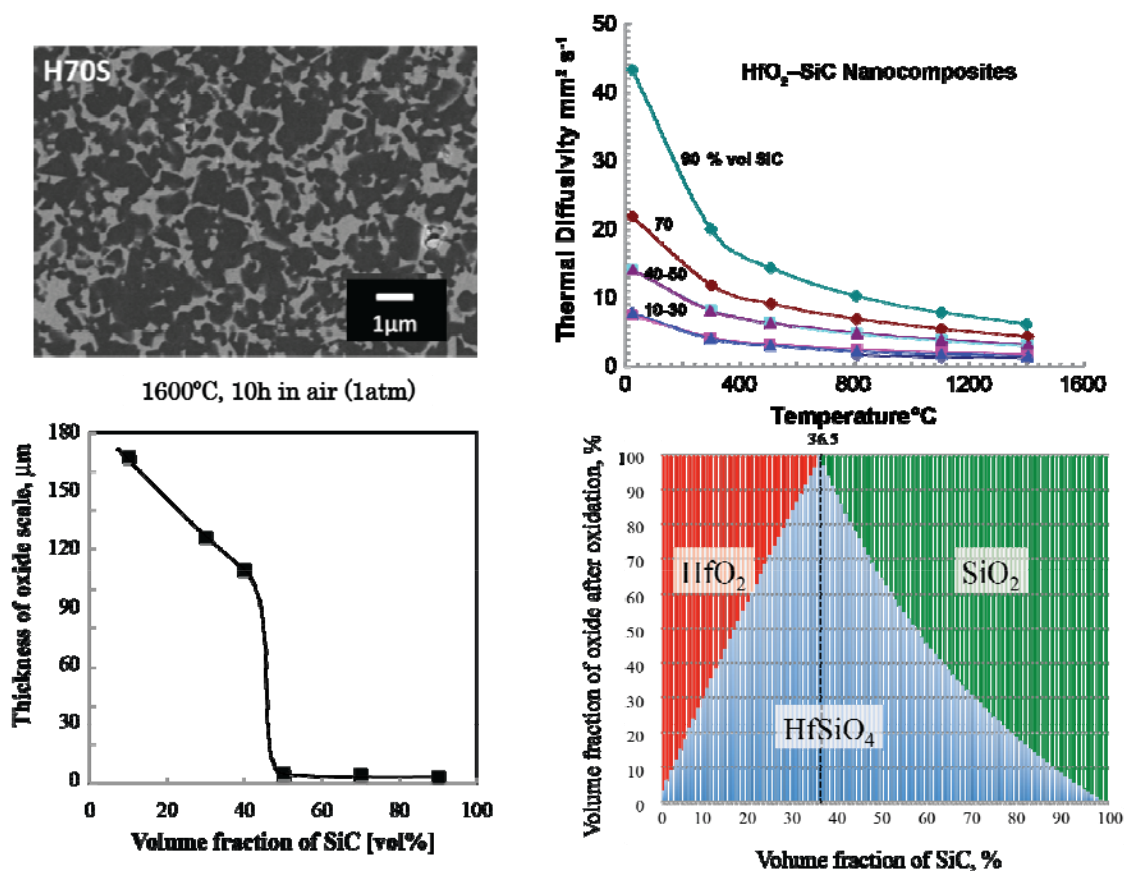*Figure 8.4: Top left: Microstructure of 70 vol% SiC (30% HfO₂) prepared by SPS. The dark phase is SiC. Top right: the non-linear increase in thermal diffusivity with the addition of SiC. Bottom left: The thickness of the oxide scale obtained at 1600 ᵒC for 10h. Bottom right: the transition to thin oxidation scale is attributed to silica rich overall composition of the composite (after oxidation of the surface layer).*

9. Ultra High Temperature Diboride Materials

Among the known UHTCs, hafnium and zirconium diboride (HfB_2 and ZrB_2) exhibit exceptional combinations of metallic, covalent and ionic bonding character. Strong covalent bonding endows them with extremely high melting temperatures (> 3200°C) as well as high hardness and elastic moduli, while metallic bonding gives them high thermal and electrical conductivities. The performance advantages of the diboride-based UHTCs derive from their high-temperature stability and high thermal conductivity. This combination of properties, along with resistance to erosion/corrosion at high temperatures, makes them potential candidates for the extreme chemical and thermal environments associated with hypersonic flight, atmospheric re-entry, and rocket propulsion systems. Other applications that take advantage of these properties include refractory linings, molten metal crucibles, plasma arc electrodes, and cutting tools. Since ZrB_2 has a lower theoretical density (6.1 g/cm^3) than HfB_2 (11.2 g/cm^3), and is also less expensive, it is often preferred over HfB_2. However, oxidation behavior is a restriction to the development of ZrB_2-based ceramics for rocket propulsion and hypersonic flight applications.

Previous studies have shown that additives such as SiC, C, B_4C, and WC accelerate densification and improve mechanical properties and oxidation resistance of ZrB_2 ceramics. The most effective additive for oxidation resistance at relatively low temperatures (800-1200°C) has been SiC and other Si-containing compounds. Formation of a protective glassy borosilicate layer impedes transport of oxygen, thereby improving oxidation resistance. Although many studies have investigated the effect of Si-containing compounds on the oxidation behavior of ZrB_2, fundamental mechanisms of oxidation of ZrB_2 with transition metal (TM) additives had not been studied previously.

The goal of this project was to study the effects of TM additives, especially W, Nb, and Mo, on the oxidation behavior of ZrB_2-based ceramics. Parameters including the type and concentration of TM additives and oxidation temperature were examined. The resulting knowledge is expected to lay the groundwork for designing ceramics that can withstand the conditions at leading edges in hypersonic vehicles. The research addressed the specific issues outlined below.

9.1 Effects of TM Additives on Oxide Scale Growth on ZrB_2

The oxidation behavior of $(Zr,Nb)B_2$ ceramics was studied to determine the effect of Nb on the thickness and morphology of the oxide scales on ZrB_2 [B6]. At 1500 °C, exposure to air resulted in the formation of a two-layer oxide scale structure on $(Zr,Nb)B_2$. The two layers were: (1) an outer layer of a glassy phase containing B_2O_3 with Nb and Zr dissolved in it; and (2) a porous oxide layer composed of oxide particles containing Zr and Nb. Small spherical particles, presumably a ZrO_2 containing dissolved Nb, grew in the glassy phase with increasing exposure time. Some of the particles were spherical while others were elongated. As the B_2O_3 evaporated, the particles became concentrated and were eventually incorporated into the newly exposed porous oxide layer, which contained both ZrO_2 and $Nb_2Zr_6O_{17}$. As the glass receded, the small precipitated particles joined the porous oxide layer that was present under the glassy layer. Because of high melting point of $Nb_2Zr_6O_{17}$ that was formed in the porous oxide layer, liquid phase sintering was not active as has been reported for W-containing ZrB_2. However, dissolution of Nb into the B_2O_3 liquid phase increased the stability of the protective liquid layer by reducing

the volatility of B_2O_3 from the liquid phase. Hence, $(Zr,Nb)B_2$ showed improved oxidation resistance compared to pure ZrB_2.

9.2 Effects of W Additives on Oxide Scale Thickness and the Protective B_2O_3 Layer

The oxidation behavior of nominally pure ZrB_2 and $(Zr,W)B_2$ ceramics with 4, 6, or 8 mol% W was studied at temperatures ranging from 800 to 1600°C [B12]. Oxidation in this temperature range resulted in the formation of a two-layer scale: (1) an outer glassy layer containing B_2O_3 with dissolved W; and (2) a porous layer composed of oxide particles containing Zr and W. Based on scale thickness and weight gain measurements, two regimes of oxidation behavior were observed. The first stage was below 1100°C for nominally pure ZrB_2 and 1300°C for $(Zr,W)B_2$ specimens. No significant differences were measured for weight loss or scale thickness between nominally pure ZrB_2 and $(Zr,W)B_2$ compositions at temperatures between 800 and 1000°C. However, the glassy layer thicknesses and weight gains were higher for $(Zr,W)B_2$ specimens after oxidation from 1100 to 1300°C. It was concluded that dissolution of W into the B_2O_3 liquid phase increased the stability of the protective liquid layer by reducing the volatility of B_2O_3 from the liquid phase, resulting in a shift in the onset of the second oxidation regime toward higher temperatures for $(Zr,W)B_2$ specimens. This assumption was confirmed by TGA analysis of B_2O_3 and B_2O_3-WO_3 glasses. Above 1500°C, the outer glassy layer was removed from the surface of nominally pure ZrB_2 by evaporation, while a thin (up to ~3μm) glassy layer was still covering the $(Zr,W)B_2$ specimens. Further, the $(Zr,W)B_2$ compositions showed lower weight gains and had thinner oxidation scales compared to nominally pure ZrB_2 at 1600°C. The addition of W into B_2O_3 increased the stability of the protective liquid/glassy layer and resulted in higher oxidation resistance for $(Zr,W)B_2$ compared to nominally pure ZrB_2.

9.3 Effects of TM Additives on Evaporation and Structural Properties of B_2O_3

The evaporation behavior of B_2O_3 with TM oxide additions was analyzed [B17]. Additions of tungsten, niobium, and zirconium oxides decreased the evaporation rate and increased the onset temperature for evaporation in B_2O_3-based glasses in the order of $WO_3 < ZrO_2 < Nb_2O_5$. High temperature Raman spectroscopy showed that WO_3 in the B_2O_3 glass was initially amorphous, but crystallized at temperatures above 500°C. In addition, the intensity of Nb_2O_5 peaks in the glass increased as a result of crystallization. No signs of formation of $BØ_4$ units was observed in the borate glasses by Raman spectroscopy or NMR. It was concluded that additions of WO_3, Nb_2O_5, or ZrO_2 to B_2O_3 did not change the structure of B_2O_3. Hence, the higher oxidation resistance of $(Zr,TM)B_2$ ceramics and lower evaporation rate of (TM-oxide)-B_2O_3 glasses should be due to the fact that the dissolution of TM-oxide in B_2O_3 decreases the activity of B_2O_3 and, consequently, decreases the vapor pressure and evaporation rate of B_2O_3.

9.4 Role of TM Selection on Oxidation of ZrB_2

The effects of additions of W, Mo, or Nb on oxidation behavior of ZrB_2 were investigated [B16]. After oxidation at 1600°C for 0 hours, the higher stability of Nb_2O_5-B_2O_3 resulted in lower oxide scale thicknesses for $(Zr,Nb)B_2$ compared to nominally pure ZrB_2 and other $(Zr,TM)B_2$ specimens. Two distinct sub-layers were observed in the porous oxide layer after oxidation at 1600°C for 6 hours, an outer layer that was lighter in color and an inner layer that was darker. The thickness of the light layer for nominally pure ZrB_2 was almost 1.5 times greater than for

$(Zr,W)B_2$ and 4 times higher than $(Zr,Mo)B_2$ and $(Zr,Nb)B_2$. Lower scale thicknesses of the light layer for $(Zr,Mo)B_2$ and $(Zr,Nb)B_2$ indicated that Mo and Nb were more effective in reducing oxygen transport from the external atmosphere toward the interface between the light and dark layers. However, the thicknesses of the dark layers were almost the same for all of the $(Zr,TM)B_2$ specimens and almost twice as thick as the dark layer for nominally pure ZrB_2, showing the same effect of TM additions on lowering the oxygen diffusion through the dark layer toward the unoxidized matrix. Additions of Mo or Nb were most effective in improving the oxidation resistance of ZrB_2 by increasing the stability of the protective liquid/glassy B_2O_3 layer and reducing the oxygen transport through the light layer.

9.5 Summary

The impact of this research was defined by the improvements in oxidation resistance of ZrB_2-based ceramics, which should also be directly applicable to other diboride ceramics. In brief, additions of TMs to ZrB_2 improve oxidation resistance as a result of the following effects:

1. TM additions decrease the evaporation rate of B_2O_3 glasses, in the order of $WO_3 < ZrO_2 < Nb_2O_5$. The effects derive from reduced activity of B_2O_3 in (TM-oxide)-B_2O_3 glasses. The increased stability of B_2O_3 glass results in an increase in the onset temperature of the transition in oxidation and lowers oxidation rates for $(Zr,TM)B_2$ relative to undoped ZrB_2.

2. Higher solubility of the TM-oxides in liquid B_2O_3 (compared to ZrO_2) promotes solution and re-precipitation of the oxides in B_2O_3 and results in thicker oxide layers with equiaxed grains. The equiaxed structure is expected to exhibit lower oxygen diffusivity than that of the columnar grains formed on undoped ZrB_2.

3. At 1600°C, the B_2O_3 layer evaporates, leaving an oxide layer composed of two sub-layers: an outer porous layer and an inner dense layer. The addition of TMs results in a decrease in the thickness of the porous layer and an increase in the thickness of the dense layer. These changes, in turn, result in lower oxygen transport and improved oxidation resistance of ZrB_2.

While the present study has elucidated some of the main effects of TMs on the oxidation behavior of ZrB_2-based ceramics, several outstanding issues remain. Resolving these issues would assist in the design of more oxidation resistant ZrB_2-based ceramics.

Which TM additives have the greatest effect on reducing the evaporation rate of B_2O_3? Since formation of binary compounds in the (TM-oxide)-B_2O_3 system is a probable reason for the reduction in the evaporation rate of B_2O_3, TM-oxides that form binary compounds with B_2O_3 should be studied. The valence numbers of the chosen TM oxides should be greater than that of Zr^{4+}; otherwise, the oxygen vacancy concentration and hence oxygen diffusivity in the zirconia oxide layer could rise.

What are the basic differences between the porous and dense oxide layers? The higher apparent density of the inner oxide layer is expected to have a lower oxygen diffusivity compared to the porous layer. In light of the fact that the dense layer can provide oxidation protection at temperatures above that at which the protective B_2O_3 layer is removed, an understanding of the fundamental differences between these layers and the role of various TMs on the stability of the dense layers could prove useful in attempts to improve oxidation resistance of ZrB_2 ceramics.

What is the effect of the TM additives on oxidation behavior of ZrB_2 in extreme environment? Since B_2O_3 glass is less stable under high air flow rates, the beneficial effects of TM additives seen in furnace studies may be altered. Testing $(Zr,TM)B_2$ specimens in more extreme environments, such as arc heaters, would provide useful information about their response in environments relevant to hypersonic flight and atmospheric re-entry.

10. List of Publications

The following is a list of publications documenting the research performed under the National Hypersonic Science Center for Materials and Structures

A. Books and book chapters

A1. D. B. Marshall and B. N. Cox (2010), "Textile Composite Materials: Ceramic Matrix," chapter in *Encyclopedia of Aerospace Engineering*, R. Blockley and W. Shyy (eds.), John Wiley & Sons Ltd., Chichester, England, pp. 2177-2188.

A2 Q. D. Yang and J. Giancaspro, "Fracture: toughness", *Encyclopedia of Composites*, editor Luigi Nicolais, Willey, 2012 (1141-1153).

A3 Q. D. Yang and B. C. Do, "Handbook of Macro to Nano Damage Mechanics", Editor, George Voyiadjis, John Wiley & Sons Ltd, 2014.

A4 Q.D. Yang and M. Naderi, "A new Augmented finite element method (A-FEM) for Analysis of Failure in advanced composite materials". Editors P. Camanho and S.R. Hallett, Woodhead Publishing Limited, to appear in 2015.

B. Papers: new materials & processing

B1 S.C. Zhang, G.E. Hilmas, and W.G. Fahrenholtz, "Oxidation of zirconium diboride ceramics with tungsten carbide additions," *Journal of the American Ceramic Society*, **94**(4) 1198-1205 (2011).

B2 W.G. Fahrenholtz and G.E. Hilmas, "Oxidation of Ultra-High Temperature Transition Metal Diboride Ceramics," International Materials Reviews 57[1] 61-72 (2012)

B3 P. Kroll, M. Andrade, X. Yan, E. Ionescu, G. Miehe, R. Riedel, "Isotropic negative thermal expansion in β-Si(NCN)$_2$ and its origin", *J. Phys. Chem.*, *J. Phys. Chem. C*, **2012**, 116, 526-531.

B4. P. Kroll, "Searching Insight into the Atomistic Structure of SiCO Ceramics," *J. Mater. Chem.* **20**, 10528-10534, 2010.

B5 J. Marschall, D.A. Pejakovic, W.G. Fahrenholtz, G.E. Hilmas, F. Panerai, and O. Chazot, "Temperature Jump Phenomenon During Plasmatron Testing of ZrB$_2$-SiC Ultra-High Temperature Ceramics," *Journal of Thermophysics and Heat Transfer*, 26[4] 559-572 (2012)

B6 M. Dehdashti, W.G. Fahrenholtz, and G.E. Hilmas, "Oxidation of Zirconium Diboride with Niobium Additions," *Journal of the European Ceramic Society*, 33(10) 1591-1598 (2013).

B7. Rishi Raj, and Susan P. Krumdieck. "A Langmuir-Kinetic Model for CVD Growth from Chemical Precursors." *Chemical Vapor Deposition* 19, no. 7-8-9 (2013): 260-266.

B8. Kalvis Terauds, and Rishi Raj. "Limits to the Stability of the Amorphous Nature of Polymer-Derived HfSiCNO Compounds." *Journal of the American Ceramic Society* 96, no. 7 (2013): 2117-2123.

B9. K. Terauds, D. B. Marshall, and R. Raj, "Oxidation of Polymer Derived HfSiCNO up to 1600°C," J. Am. Ceram.Soc., 96 [4] 1278–1284 (2013).

B10. B. Xu, P. Kroll, "Oxidation mechanisms of SiCO ceramics: first principles study on diffusion and reactionof O$_2$" submitted to Phys. Rev. B.

B11. Rishi Raj, "Chemical Potential-Based Analysis for the Oxidation Kinetics of Si and SiC Single Crystals." *Journal of the American Ceramic Society* 96, no. 9 (2013): 2926-2934.

B12. M. Kazemzadeh Dehdashti, W.G. Fahrenholtz, and G.E. Hilmas, "Effects of Temperature and the Incorporation of W on the Oxidation of ZrB$_2$ Ceramics," *Corrosion Science*, 80 221-228 (2014).

B13. Aziz I. Abdulagatov, Kalvis E. Terauds, Jonathan J. Travis, Andrew S. Cavanagh, R. Raj and Steven M. George, "Pyrolysis of Titanicone Molecular Layer Deposition Films as Precursors for Conducting TiO2/Carbon Composite Films," J. Phys. Chem. (submitted May 2013)

B14. Kalvis Terauds, Rishi Raj, and Peter Kroll. "Ab inito and FTIR Studies of HfSiCNO Processed from the Polymer Route." *Journal of the American Ceramic Society* 97, no. 3 (2014): 742-749.

B15. Y. Shinoda, D. B. Marshall and R. Raj, "Oxidation, Mechanical and Thermal Properties of Hafnia-Silicon Carbide NanoComposites." J. Eur. Ceram. Soc. 34[7] 1783–1790 (2014)

B16. M. Kazemzadeh Dehdashti, W.G. Fahrenholtz, and G.E. Hilmas, "Effects of Transition Metals on the Oxidation Behavior of ZrB$_2$ Ceramics," submitted for publication in *Corrosion Science* on July 13, 2014 and is currently in review

B17. M. Kazemzadeh Dehdashti, A. Mohammadkhah, W.G. Fahrenholtz, and G.E. Hilmas, "Effect of Transition Metal Oxide Additions on the Structure of B$_2$O$_3$ Glasses," to be submitted to the journal *Corrosion Science*.

B18. Kalvis Terauds, Kalvis, and Rishi Raj. "Dramatic influence of interface chemical potentials on the oxidation of silicon and carbon based compounds." *Journal of the European Ceramic Society* 34, no. 4 (2014): 1035-1039.

B19. Rishi Raj and Kalvis Terauds, "Oxidation Map for SiC Displays Regime of Bubble Nucleation," submitted to *Journal of the American Ceramic Society*, July 2014.

B20. Nelli Bodifort and Peter Kroll, "Crystalline Approximants of Silicon Oxycarbide Ceramics," to be submitted to J. Eur. Ceram. Soc.

B21. Atreyi Dasmahapatra and Peter Kroll, "Ab Inito Simulations of Structure and Thermodynamic Properties of Hafnia-Silicate Glasses," to be submitted to J. Non-Cryst. Solids.

B22. John P. Nimmo and Peter Kroll, "First-Principles Calculations and Analysis of 29Si Nuclear Magnetic Resonance Chemical Shifts in Silicon Oxycarbide Ceramics", submitted to J. Phys. Chem. C.

C. Papers: multiscale modeling & virtual test

C1. Q. D. Yang, B. N. Cox, X. J. Fang, and Z. Q. Zhou, "Virtual testing for advanced aerospace composites: advances and future needs," *Journal of Engineering Materials Technology*, **133** (11001-11006),, 2011.

C2. Q. D. Yang, X. J. Fang, J. X. Shi and J. Lua, "An improved cohesive element for shell delamination analyses," *International Journal for Numerical Methods in Engineering*, **83**(5), 611-641, 2010.

C3. X. J. Fang, Q. D. Yang, B. N. Cox, and Z. Q. Zhou. "An augmented cohesive zone element for arbitrary crack coalescence and bifurcation in heterogeneous materials", *International Journal for Numerical Methods in Engineering,* **88** (841-861) 2011.

C4. X. J. Fang, Z. Z. Zhou, B. N. Cox and Q. D. Yang, "High-fidelity simulations of multiple fracture processes in laminated composites in tension," *Journal of the Mechanics and Physics of Solids*, **59** (1355-1373), 2011.

C5. H. Qiao, Q. D. Yang, W. Q. Chen, and C. Z. Zhang, "Implementation of the Arlequin method into ABAQUS: Basic formulation and applications," *Advances in Engineering Software*, **42** (197-207), 2011.

C6. H. Bale, M. Blacklock, M. Begley, R. O. Ritchie, D. B. Marshall, and B. N. Cox, "Characterizing three-dimensional textile ceramic composites using synchrotron x-ray micro-computed-tomography," *Journal of the American Ceramic Society*, 95[1] 392-402 (2012).

C7. M. Blacklock, H. Bale, M. Begley, and B. N. Cox, "Generating virtual textile composite specimens using statistical data from micro-computed tomography: 1D tow representations for the Binary Model", *J. Mech. Phys. So*lids, **60** [3] 451–470 (2012).

C8. R.G. Rinaldi, M. Blacklock, H. Bale, M.R. Begley, B.N. Cox, "Generating virtual textile composite specimens using statistical data from micro-computed tomography:3D tow representations,", *J. Mech. Phys. Solids*, 60[8] 1561-1581 (2012).

C9. A. Vanaerschot, B. N. Cox, S. V. Lomov, D. Vandepitte."Stochastic framework for quantifying the geometrical variability of laminated textile composites using micro-computed tomography," *Composites A*, 44[1] 122-131 (2013).

C10. A. Vanaerschot, B. N. Cox, S. V. Lomov, D. Vandepitte, "Stochastic multi-scale modelling of textile composites based on internal geometry variability," *Computers and Structures*, 122[6] 55-64 (2013).

C11. Q. D. Yang, "A Novel Nonlinear Solving Algorithm for Advanced Finite Element Methods with Embedded Cohesive Cracks", Computer Method in Applied Mechanics and Engineering, submitted. 2014

C12. W. Liu, B. C. Do, Q. D. Yang, and X. Y. Su, "Improved Cohesive Stress Integration Schemes for Cohesive Zone Elements", Engineering Fracture Mechanics, 107 14-28, (2013).

C13. Q. D. Yang, X. J. Fang, W. Liu, and B. N. Cox, "High-fidelity Analyses of composites at various length scales with discrete damage representations", Journal of Multifunctional Composites, Vol **1** (1-14), 2013.

C14. W. Liu, Q. D. Yang, et al., "An Accurate and Efficient A-FEM for Arbitrary Crack Interactions", ASME Journal of Applied Mechanics, 80 041033-1 to 041033-12 (2013).

C15. W. Liu, Q. D. Yang, et al., "An Efficient Augmented Finite Element Method (A-FEM) for Arbitrary Cracking and Crack Interaction in Solids", International Journal for Numerical Methods in Engineering, 99 438-468 (2014).

C16. M. Naderi and Q. D. Yang, "Augmented Finite Element Method for Arbitrary Cracking in 3D Solids", International Journal for Numerical Methods in Engineering, to be submitted. 2013,

C17. V. Rajan, F.W. Zok, "Remediation of a constitutive model for ceramic composite laminates", *Composites A*, in press.

C18. B.N. Cox, H.A. Bale, M. Begley, M. Blacklock, B-C Do, T. Fast, M. Naderi, M. Novak, V. P. Rajan, R. G. Rinaldi, R. O. Ritchie, M. N. Rossol, J. H. Shaw, O. Sudre, Q. Yang, F.W. Zok, and D.B. Marshall, "Stochastic Virtual Tests for High-Temperature Ceramic Matrix Composites," Annu. Rev. Mater. Res. 44:479-529 (2014)

C19. A. Vanaerschot, B.N. Cox, S.V. Lomov and D. Vandepitte, "Simulation of the cross-correlated positions of in-plane tow centroids in textile composites based on experimental data," *Composite Structures*, 116, 75-83 (2014).

C20. F.B. Tu, D.S. Ling, L.F. Bu, and Q. D. Yang, "Generalized bridging domain method for coupling finite element methods with discrete elements", Computer Methods in Applied Mechanics and Engineering, 276 (509-533), 2014.

C21. B.C. Do and Q.D. Yang, "AFEM for arbitrary cracking in solids under general thermal-mechanical loadings". International Journal of Numerical Methods in Engineering, to be submitted.

C22. A. Fast, A. E. Scott, H. A. Bale, and B. N. Cox, "Topological and Euclidean descriptors for imperfect fiber bundles," in preparation for submission to *Journal of the Mechanics and Physics of Solids*.

C23 Naderi, M., D. Schesser, et al. (2014). "Augmented finite element method for arbitrary cracking in 3D solids." *International Journal of Fracture* submitted.

D. Papers: experimental tools & property measurement

D1. S. Lucato, O.H. Sudre, and D.B. Marshall, "A Method for Assessing Reactions of Water Vapor with Materials in Combustion Environments," *Journal of the American Ceramic Society*, 94[S1] S186-S195 (2011)

D2. M. Novak and F.W. Zok (2011). "High-Temperature Materials Testing with Full-field Strain Measurement: Experimental Design and Practice." *Review of Scientific Instruments* **82**, 115101 (2011).

D3. V. Rajan, M. Rossol and F.W. Zok (2011). "Optimization of digital image correlation measurements for high-resolution strain mapping of woven composites," *Experimental Mechanics*, DOI 10.1007/s11340-012-9617-1 April 2012.

D4. R. Miles, P. Howard, C. Limbach, S. Zaidi, S. Lucato, B. Cox, D.B. Marshall, A.M. Espinosa, D. Driemeyer "A Shape Morphing Ceramic Composite for Variable Geometry Scramjet Inlets," *Journal of the American Ceramic Society*, 94[S1] S35-S41 (2011)

D5. V.P. Rajan, F.W. Zok, "Effects of non-uniform strains on tensile fracture of fiber-reinforced ceramic composites", *Journal of Mechanics and Physics of Solids*, in press.

D6 H.A. Bale , A. Haboub , A.A. MacDowell, J.R. Nasiatka, D.L. Parkinson, B.N. Cox , D.B. Marshall and R.O. Ritchie, "Real-Time Quantitative Imaging of Failure Events in Materials under Load at Temperatures above 1600°C," *Nature Materials,* 12[1] 40-46 (2013)

D7. Michael N. Rossol, John Shaw, Hrishikesh Bale, Robert O. Ritchie, David B. Marshall, Frank W. Zok, "Characterizing weave geometry in textile ceramic composites using digital image correlation," J. Am. Ceram. Soc., vol. 96 [8], 2362-2365 (2013)

D8 J. H. Shaw, V. P. Rajan, M. Blacklock, F. W. Zok , "Towards Virtual Testing of Textile Composites: Calibration of Thermoelastic Tow Properties", Journal of the American Ceramic Society, 97 [4] 1209–1217 (2014).

D9 M. N. Rossol, T. Fast, D. B. Marshall, B. N. Cox, F. W. Zok, "Characterizing in-plane geometrical variability in textile ceramic composites," J. Am. Ceram. Soc., in press.

D10 J. H. Shaw, M. N. Rossol, D. B. Marshall, F. W. Zok, "Effects of Tow-Scale Holes on the Mechanical Performance of a 3D Woven C/SiC Composite," J. Am. Ceram.Soc. in review

D11. A. Haboub, H. A. Bale, J. R. Nasiatka, B. N. Cox, D. B. Marshall, R. O. Ritchie, A. A. MacDowell, "Tensile Testing of Materials at High Temperatures above 1700°C with In Situ Synchrotron X ray Micro-Tomography," Rev. Sci Inst., 85 [8] 083702 (2014)

D12 J.H. Shaw, M.N. Rossol, D.B. Marshall, F.W. Zok, "Effects of Fabric Shear on the Mechanical Performance of a 3D Woven C/SiC Composite", submitted to J. Am. Ceram. Soc. (2014).

D13 V.P. Rajan, J.H. Shaw, F.W. Zok, "An elastic-plastic constitutive model for ceramic composite laminates", *Composites Part A*, in press (2014).

Conference Proceedings

E1. Q. D. Yang, X. J. Fang, Z. Q. Zhou and B. N. Cox, "A-FEM for complex multi-scale damage evolution in laminated composites", p 1-8, International SAMPE Technical Conference. May, 2010.

E2. C. Roux, Q. D. Yang and B. N. Cox, "Modeling arbitrary multiple cracks in 3D textile composites using hybrid BM and A-FEM formulation," Proceedings of USNCTAM2010. Paper No.412. Penn State, June, 2010.

E3. X. J. Fang, Q. D. Yang, J. X. Shi and J. Lua, "An Improved Cohesive Element for Shell Delamination Analyses," Proceedings of USNCTAM2010. Paper No. 414, Penn State, June, 2010.

E4. Q. D. Yang, X. J. Fang, and B. N. Cox, "Numerical simulation of composites at various length scales: where are the limits," *Proceedings of 32nd Risoe International Symposium on Material Science – Composite materials for structural performance: towards higher limits.* Editors: S. Faester, J. Jensen, R. Ralph, and B. F. Sorensen. p. 179-196. Roskilde, Denmark, Sept 5-9, 2011 (keynote paper).

E5. B. N. Cox, M. R. Begley, P. Kroll, D. B. Marshall, R. O. Ritchie, and Q. D. Yang, "Multi-Scale Approaches to Fracture and Fatigue of Fiber Composites – Where Are the Experimental and Computational Limits and Challenges?," *Proceedings of the 32nd International Riso Symposium*, Denmark, September, 2011.

E6. B. Kouchmeshky, P. Kroll and I. Olubanjo, "Optimized Design of Composite Materials for Heat Transport Applications," for Proceedings of the ASME 2011 International Mechanical Engineering Congress & Exposition, ASME 2011, November 11-17, 2011, Denver, Colorado, USA

E7. B. Kouchmeshky and P. Kroll, "Quantifying Thermal Transport of High-Temperature Ceramics from First Principles Calculations," for Proceedings of the ASME 2011 International Mechanical Engineering Congress & Exposition, ASME 2011, November 11-17, 2011, Denver, Colorado, USA

E8. Q. D. Yang and X. J. Fang, "A-FEM and It's Applications in Modeling Progressive Damage Evolution in Heterogeneous Materials," USNCCM 2011, July 22-29, Minneapolis, MN.

E9 A. Vanaerschot, B. N. Cox, M. Blacklock, G. Kerckhofs, M. Wevers, S.V. Lomov, D. Vandepitte. "Statistical description of the internal geometry of a polymer textile composite using micro-computed tomography" in *Proc. 15th European Conference on Composite Materials, Venice, Italy, June, 2012, (ECCM-15), ISBN 978-88-88785-33-2, (2012)*.

E10. A. Vanaerschot, B. N. Cox, S. V. Lomov, D. Vandepitte. "Mechanical property evaluation of polymer textile composites by multi-scale modelling based on internal geometry variability," *Proceedings of the ISMA2012-USD2012, pp. 5053-5064, Leuven, Belgium, September 2012*

E11. X. J. Fang, Z. Q. Zhou, and Q. D. Yang, "A-FEM for Nonlinearly Coupled Multiple Cracking in Laminated Composites", Proceedings of USNCTAM2010, paper No. USNCTAM2010-413. 2010.

E12. Q. D. Yang, R. Mohammadizadeh, and B. N. Cox, "Weight function based microscopic elements for multiscale A-FEM analysis of composites without hierarchical homogenization", Proceedings of International SAMPE Conference 2012, pp 1-8, Baltimore, MA. May 2012.

E13. Q. D. Yang, "Explicit Multi-scale Damage Modeling for Virtual Testing of Composite Materials", Proceedings of Structural Integrity and Fracture (SIF2013) conference, Melbourne, Australia. July 11-12, 2013 (keynote paper).

E14. Q. D. Yang, W. Liu, and X. Y. Su, "An efficient A-FEM for Arbitrary Cracking in Solids", Proceedings of International Congress of Fracture (ICF2013), Beijing, China, June16-21, 2013.

E15. Brian Cox, Hrishikesh Bale, Matthew Blacklock, Bao-Chan Do, David Marshall, Robert Ritchie, Qingda Yang, Frank Zok, Renaud Rinaldi, "A Pipeline Approach to Developing Virtual Tests for Composite Materials," Proceedings of 13th International Conference on Fracture, June 16–21, 2013, Beijing, China.

E16. Q. D. Yang and D. S. Ling, "Advanced Numerical Methods for Progressive Damage Evolution Analyses of Heterogeneous Materials", Symposium on Recent Advances in Solid Mechanics and Applications, August 14-16, Hangzhou, China.

E17. Cox, B. N., Bale, H. A., Blacklock, M., Fast, T., Novak, M., Rajan, V., Rinaldi, R., Ritchie, R. O., Rossol, M., Shaw, J., Yang, Q. D., Zok, F., and Marshall, D. B., "Stochastic virtual test systems for ceramic composites," in Proceedings of the *11th International Conference on Textile Composites (TexComp11)*, Leuven, Belgium, September 19-20, 2013.

E18. Vanaerschot A., Cox B.N., Lomov S.V., Vandepitte D., "Stochastic characterisation of the in-plane tow centroid in textile composites to quantify the multi-scale variation in geometry," in *Proceedings of the IUTAM Symposium on Multiscale Modeling and Uncertainty Quantification of Materials and Structures, Santorini, Greece, September 8-11,* 2013. pp. 187-202, Springer (2014).

E19. Vanaerschot A., Cox B.N., Lomov S.V., Vandepitte D., "Stochastic modelling of the geometrical variability in textile composites using experimental data," in *Proceedings of the International Conference on Uncertainty in Structural Dynamics (USD 2014)*. Leuven, Belgium, September 15-17, 2014.

E20. Vanaerschot A., Cox B.N., Lomov S.V., Vandepitte D. "Stiffness evaluation of polymer textile composites subjected to internal geometry variability," in *SAMPE 2013 Proceedings: Education & Green Sky - Materials Technology for a Better World. Long Beach, USA*, May 6-9, 2013, pp. 2630-2644 (2013).

E21. Vanaerschot A., Cox B.N., Lomov S.V., Vandepitte D., "Generation of stochastic macroscopic structures using experimental data of random geometry," in *Proceedings of the 11th International Conference on Textile Composites (TexComp11), Leuven, Belgium,* September 19-20, 2013.

E22. Vanaerschot A., Cox B.N., Lomov S.V., Vandepitte D. "Stochastic multi-scale modelling of short- and long-range effects in textile composites based on experimental data," in *Proceedings 16th European Conference on Composite Materials. Seville, Spain,* June 22-26, 2014.

E23. Vanaerschot A., Cox B.N., Lomov S.V., Vandepitte D., "Stochastic multi-scale modelling of composite materials based on experimental data," in *Proceedings of the International Conference on Structural Dynamics (EURODYN2014), Porto, Portugal,* June 30-July 2, 2014.

E24. M. Blacklock, F.W. Zok, B.N. Cox, "A voxel-based approach to meshing woven fibre composites", in *Proceedings of 8th Australasian Congress on Applied Mechanics*, 2014.

11. List of Participants

Program Management

The National Hypersonic Science Center for Materials and Structures (NHSC-MS) was funded jointly by the Air Force Office of Scientific Research and NASA. The program managers at AFOSR and NASA were Ali Sayir (AFOSR) and Anthony Calomino (NASA)

The technical NHSC-MS program was led by Teledyne Scientific Company (PI David Marshall), with subcontracts to the following team members: University of California, Berkeley (PI R. Ritchie); University of California, Santa Barbara (PI F. Zok); University of Colorado, Boulder (PI R. Raj); University of Miami (PI Q. Yang); University of Texas, Arlington (PI P. Kroll); and Missouri University of Science and Technology (PI G. Hilmas & W. Fahrenholtz).

A governing board, consisting of representatives from AFRL and NASA, reviewed the technical program annually and provided valuable technical guidance. The board members were as follows: Chad Hunter (AFRL), Thomas Eason (AFRL), Kim Bey (NASA), Harry Partridge (NASA), David Mollenhauer (AFRL), and Lawrence Matson (AFRL).

Additional valuable technical guidance was provided by an Advisory Board, who participated in various technical meetings, including the annual program reviews, annual winter planning workshops held at the University of California, Santa Barbara, a summer school held at the University of California, Santa Barbara, and workshop/conferences held at the University of Colorado, Boulder. The members were: Dan Driemeyer (Boeing), Brian Zuchowski (Lockheed-Martin), Greg Morscher (University of Akron)

Technical Participants

The research summarized in this report was performed by the following participants of the NHSC-MS:

Teledyne Scientific Company
PI: David Marshall, Brian Cox
Research staff: Olivier Sudre, M. Calabrese

University of Texas, Arlington
PI: Peter Kroll
Post Doctoral Fellows: Babak Kouchmeshky, Ningbo Liao, Bin Xu, Christine Morrow, Jean Njoroge, Thiruvillamala Mahadevan
Graduate students: Ibukun Olubango, Munuve Mwania, Nelli Bodiford, John Nimmo, Atreyi Dasmahapatra, John Nimmo, Atreyi Dasmahapatra, Atreyi Dasmahapatra, John Nimmo

Missouri University of Science and Technology
PI: Greg Hilmas & William Fahrenholtz
Post Doctoral Fellows: Shi Zhang, Jeremy Watts
Graduate students: Maryam Dehdashti, Alex Olp, Jeremy Watts

University of Colorado, Boulder
PI: Rishi Raj
Post Doctoral Fellows: Jianhong Shen, Lung-hao Hus
Graduate students: Kalvis Terauds, Jason Lonergan

University of California, Berkeley
PI: Rob Ritchie
Post Doctoral Fellows: Hrishkesh Bale

University of Miami
PI: Qingda Yang
Post Doctoral Fellows: Xiujun Fang, Mehdi Naderi
Graduate students: Bao-Chan Do, Reza Mohammadizadeh , Derek Schesser, Brigitte Morale

University of California, Santa Barbara
PI: Frank Zok
Post Doctoral Fellows: Matthew Blacklock, Tony Fast, Renaud Rinaldi, Shahram Amini, Mark Novak
Graduate students: John Shaw, Michael Rossol, Varun Rajan, Matt Reinhold

Other Technical Collaborations

AFRL: A parallel program at AFRL on materials for hypersonics was funded by AFOSR. Participants in this program participated in all the NHSC planning workshops and reviews. They also provided supporting collaborations and testing of materials. The participants were Michael Cinibulk, Triplicane Parthasarathy, Randy Hay

Advanced Light Source (ALS) / Lawrence Berkeley National Laboratory (LBNL): Synchrotron beam time was provided by ALS. Support for design and construction of the in situ high-temperature μ-CT loading stage was provided by Alastair A. MacDowell, Abdel Haboub, and James R. Nasiatka.

The NHSC enabled more than 12 active and ongoing collaborations to be established with researchers from universities and laboratories worldwide (Britain, Europe, Japan, New Zealand, and Australia). These are listed in the annual review presentations.